



Regulation of Star Formation by a Hot Circumgalactic Medium

Christopher Carr¹, Greg L. Bryan^{1,2}, Drummond B. Fielding², Viraj Pandya^{2,3,4}, and Rachel S. Somerville²¹Department of Astronomy, Columbia University, 550 West 120th Street, New York, NY 10027, USA; cc4504@columbia.edu²Center for Computational Astrophysics, Flatiron Institute, New York, NY 10010, USA³Columbia Astrophysics Laboratory, Columbia University, 550 West 120th Street, New York, NY 10027, USA

Received 2022 November 7; revised 2023 March 10; accepted 2023 March 12; published 2023 May 23

Abstract

Galactic outflows driven by supernovae (SNe) are thought to be a powerful regulator of a galaxy’s star-forming efficiency. Mass, energy, and metal outflows (η_M , η_E , and η_Z , here normalized by the star formation rate, the SNe energy, and metal production rates, respectively) shape galaxy properties by both ejecting gas and metals out of the galaxy and by heating the circumgalactic medium (CGM), preventing future accretion. Traditionally, models have assumed that galaxies self-regulate by ejecting a large fraction of the gas, which enters the interstellar medium (ISM), although whether such high mass loadings agree with observations is still unclear. To better understand how the relative importance of ejective (i.e., high mass loading) versus preventative (i.e., high energy loading) feedback affects the present-day properties of galaxies, we develop a simple gas-regulator model of galaxy evolution, where the stellar mass, ISM, and CGM are modeled as distinct reservoirs which exchange mass, metals, and energy at different rates within a growing halo. Focusing on the halo mass range from 10^{10} to $10^{12} M_\odot$, we demonstrate that, with reasonable parameter choices, we can reproduce the stellar-to-halo mass relation and the ISM-to-stellar mass relation with low-mass-loaded ($\eta_M \sim 0.1$ – 10) but high-energy-loaded ($\eta_E \sim 0.1$ – 1) winds, with self-regulation occurring primarily through heating and cooling of the CGM. We show that the model predictions are robust against changes to the mass loading of outflows but are quite sensitive to our choice of the energy loading, preferring $\eta_E \sim 1$ for the lowest-mass halos and ~ 0.1 for Milky Way-like halos.

Unified Astronomy Thesaurus concepts: [Circumgalactic medium \(1879\)](#); [Galactic winds \(572\)](#); [Galaxies \(573\)](#); [Galaxy evolution \(594\)](#); [Galaxy physics \(612\)](#); [Galactic and extragalactic astronomy \(563\)](#)

1. Introduction

Early theories of galaxy formation proposed that galaxies form from cooling gas that sinks to the centers of virialized dark matter halos and self-gravitates to form stars (White & Rees 1978). However, early models ran into the longstanding problem of “overcooling,” where the accretion of gas in halos form galaxies that are too efficient at producing stars, particularly in low-mass and high-mass halos (Dekel & Silk 1986; White & Frenk 1991). This manifests as a mismatch in the stellar-to-halo mass relation, which compares the typical stellar masses in galaxies in the real universe to their respective dark matter halos via abundance-matching techniques (Moster et al. 2010; Behroozi et al. 2019).

Later generations of galaxy formation modeling have attempted to address this problem of overcooling by introducing feedback from supernovae (SNe) explosions to make star formation less efficient in Milky Way (MW) and lower-mass halos (Somerville & Davé 2015). Massive stars upon their death deposit enormous quantities of energy, enriched gas, and momentum into the surrounding interstellar medium (ISM), regulating star formation by providing a source of effective pressure that counterbalances the local disk weight, supporting the disk against gravitational collapse (e.g., Thompson et al. 2005; Ostriker & Kim 2022). However, feedback not only regulates star formation within the ISM, by introducing a

source of heating and turbulence (Krumholz et al. 2009), but also through its ability to drive large-scale multiphase outflows with mass-loss rates comparable to the galaxy’s star formation rate, quantified by the mass-loading factor, η_M (Heckman et al. 1990; Strickland & Stevens 2000; Strickland & Heckman 2009). The presence of these galactic winds has been confirmed by observations of outflows in star-forming galaxies at high and low redshift (for reviews, see Veilleux et al. 2005 and Rupke 2018). Once these outflows leave the ISM, their mass, energy, and metals are either deposited into the circumgalactic medium (CGM; Heitsch & Putman 2009), recycled and accreted back onto the disk in a “galactic fountain” (Shapiro & Field 1976; Bregman 1980; Marasco et al. 2022), or even driven out of the halo entirely (Oppenheimer & Davé 2008; Kereš et al. 2009; Oppenheimer et al. 2010). SNe feedback, which is the focus of this work, is important but insufficient to explain the observed star formation inefficiencies and outflows in halos with masses $\gtrsim 10^{12} M_\odot$, and thus requires additional feedback from active galactic nuclei (AGNs; Benson et al. 2003; Croton et al. 2006; Somerville et al. 2008; Benson 2010).

Efforts to properly model these baryon flows on galactic scales typically rely on two broad categories of techniques. The most direct way involves numerical hydrodynamic simulations that explicitly track gravity and gas dynamics for particles or grid cells representing baryons and dark matter. Despite the ability to make detailed predictions, an immediate downside to this technique is that it is quite computationally expensive and, except possibly for the smallest galaxies, does not possess the necessary resolution to trace individual SNe remnants or properly track the evolution of diffuse, multiphase galactic winds. These simulations must then rely on simplified physical

⁴ Hubble Fellow.

subgrid models to follow the physics on scales that are not resolved; these subgrid models are generally calibrated to reproduce observed galaxy scaling relations or related observables (e.g., Oppenheimer & Davé 2006; Vogelsberger et al. 2014; Crain et al. 2015; and the reviews by Naab & Ostriker 2017 and Vogelsberger et al. 2020). A less costly alternative is semi-analytic modeling (or semi-analytic models, SAMs; e.g., White & Rees 1978; White & Frenk 1991; Kauffmann et al. 1993; Somerville & Primack 1999; Cole et al. 2000; Baugh 2006; Somerville et al. 2008; and the reviews by Benson 2010 and Somerville & Davé 2015). Rather than simulating the hydrodynamics directly, SAMs track numerous interlocking physical processes in the build up of galaxies based on the underlying dark matter merger tree using parameterized recipes. This method is relatively fast and can efficiently explore different parameter choices, but it too has its drawbacks, as SAMs can quickly become quite complex and rely on a host of free parameters that are not well constrained.

Despite these differences in techniques in galactic modeling, something that has been common among them is their reliance on strong stellar feedback to reduce the galactic baryon fraction and the overall stellar mass. Large cosmological simulations that lack the spatial resolution to model wind generation generally require a significant ejection of mass out of the galaxy in order to match observed galaxy statistics, and a steep dependence on halo mass or circular velocity to match the stellar-to-halo mass relation and the low-mass-end slope of the stellar mass function (Somerville & Davé 2015). For example, large-scale cosmological simulations such as Illustris-TNG (Pillepich et al. 2018) or SIMBA (Davé et al. 2019) explicitly impose high-mass-loaded winds, although there are a few exceptions, such as EAGLE (Schaye et al. 2014), which injects high-specific-energy feedback instead. High-mass outflow rates also appear in higher-resolution “zoom-in” cosmological simulations such as FIRE, which aim to produce galactic winds self-consistently (Muratov et al. 2015; Pandya et al. 2021). Mass loadings can be even higher in SAMs (10–100 times greater than the FIRE estimates) in order to compensate for the similarly larger gas accretion rate into low-mass galaxies (Pandya et al. 2020).

However, this “traditional” approach to achieving low stellar-to-halo mass fractions, by assuming that galaxies eject a large fraction of the gas which enters the disk, has come into growing tension from two directions: (i) observations of galactic winds from low-mass galaxies, and (ii) high-resolution simulations of self-consistently driven winds.

Observationally derived mass-loading estimates for star-forming galaxies with stellar masses from $10^7 < M_*/M_\odot < 10^{11}$ using UV absorption-line measurements from the Cosmic Origins Spectrograph on board the Hubble Space Telescope (HST-COS) find η_M values in the range of 1–10 with a negative correlation with stellar mass (Chisholm et al. 2017). Recent deep H α observations from McQuinn et al. (2019) of the low-surface-brightness features of galactic winds from a sample of 12 low-mass galaxies derive mass loadings on the order of 0.2–7. They find that the majority of the ejected wind from the dwarfs remain in the halo and, consistent with Martin (1999), find a much weaker dependence on circular velocity or stellar mass than what is generally adopted in cosmological simulations. Another study, from Marasco et al. (2023), using H α kinematics find even smaller estimates for mass-loading factors for gas that escapes the halo, reporting values as small

as $\log_{10} \eta_M \sim -2$ for systems with stellar masses from $10^7 < M_*/M_\odot < 10^{10}$. The results from Marasco et al. (2023) appear in line with similarly low-outflow-rate estimates from Concas et al. (2022) at higher redshift ($1.2 < z < 2.6$) using stacked emission-line data from the KLEVER survey. However, current estimates of wind outflow rates and mass loadings from observations are subject to large uncertainties, due to the unknown geometry of the wind as well as the difficulty of observing all phases of the wind (e.g., Tripp et al. 2011).

On the simulation side, another approach to modeling galactic winds is via “small-scale” simulations that resolve patches of the ISM down to the \sim parsec scale and can resolve the Sedov–Taylor phase of expanding SNe remnants and their interaction with the ISM, which is crucial to resolving the multiphase nature of galactic winds (e.g., Girichidis et al. 2016; Li et al. 2017; Kim et al. 2020). These simulations can track outflows of mass and energy of each phase of the wind, which reach different heights from the disk as a function of gas and star formation rate densities. The consensus picture emerging from these ISM patch simulations is that the hot phase ($T \sim 10^6$ K) carries most of the energy, while the cold phase ($T \sim 10^4$ K) carries most of the mass (Fielding et al. 2018; Kim et al. 2020; Li & Bryan 2020). Since outflows measured in these simulations are much closer to the disk and represent a small patch of the ISM, they cannot be directly compared to observations. Mass loadings in the cool phase measured at the disk scale height can be as high as 1–100 times the star formation rate and decrease with star formation density. However, most of this cool gas is moving at low velocities, meaning that the mass loading of cooler outflows declines precipitously with increasing height from the galaxy, as cool gas that cannot escape the galaxy’s potential falls back to the disk. The energy outflows in the hot phase of the wind, possessing a specific energy an order of magnitude larger than the cold phase, carry about $\sim 10\%$ of the energy ejected from SNe. This is enough energy to break out from the ISM and reach greater heights from the galaxy, often with Bernoulli velocities greater than the galaxy escape velocity (Kim et al. 2017, 2020). Lastly, there are high-resolution simulations of dwarf galaxies which also find lower-mass-loaded winds beyond the virial radius than what is adopted in cosmological simulations (Hu 2019).

These hot winds may not eject much mass out of the galaxy, but the energy they contain may contribute to a *preventative* aspect of SNe feedback. Instead of only an ejective mode, energy flux from galactic winds can heat up circumgalactic material, preventing further radiative cooling in the gas and reducing the ambient density of the CGM by lifting gas to greater altitudes through gradual heating (Voit et al. 2017). This heating from a central feedback source, either from SNe or a central black hole in more massive galaxies, has been proposed as a means to regulate subsequent star formation by not only removing baryons from the CGM, preventing them from accreting onto the galaxy in the first place, but also by keeping gas in the CGM in a quasi-equilibrium state where precipitation of cold gas clouds via thermal instabilities out of a hot gaseous halo and accretion onto the disk is limited by the ratio between the cooling time, t_{cool} , and the freefall time, t_{ff} (Sharma et al. 2012a, 2012b; McCourt et al. 2012; Voit et al. 2015a, 2015b, 2017). These SN-driven winds that escape from halos (or lifted CGM gas through heating) may also shock-heat gas beyond the CGM and thereby prevent cosmic accretion

(Pandya et al. 2020). The combination of mounting observations favoring lower-mass outflows than what is required in cosmological simulations and the emerging view from small-scale simulations emphasizing the multiphase nature of galactic winds may call for a rethinking of how galaxies regulate their growth, and whether that regulation is primarily ejective or preventative in nature.

In this paper we examine this question using a simplified method that is distinct from numerical simulations and even more stripped down than traditional SAMs for modeling the process of galaxy formation. These models have come to be known as “gas-regulator” or “bathtub” models (e.g., Bouche et al. 2010; Dekel et al. 2013; Lilly et al. 2013). Explored extensively in prior works (Davé et al. 2012; Birrer et al. 2014; Dekel & Mandelker 2014; Peng & Maiolino 2014; Mitra et al. 2015; Furlanetto 2021; Furlanetto & Mirocha 2022), these regulator models use simple (but physically based) analytic arguments and approximations to model gas flows and the conversion of gas into stars. The components of the galaxy are treated as mass reservoirs (“bathtubs”) which exchange mass and metals at different rates. The base framework comes from a simple set of differential equations that describes the flows between the various reservoirs. Sometimes, but not always, an equilibrium condition is also added, which states that the inflow of mass from the intergalactic medium (IGM) into the ISM balances the sum of gas mass lost from outflows and converted into stars (e.g., Finlator & Davé 2008). Usually, a galaxy is assumed to evolve without mergers, with the mass inflow of dark matter and baryons set by fits to average mass accretion histories extracted from dissipationless N -body simulations. An advantage of these models is that they are simple, making clear the physical underpinnings that connect the reservoirs, and converge to solutions that are independent of initial conditions. Although gas-regulator models are not meant to replace their more sophisticated cousins like SAMs or hydrodynamical simulations, these models have proved to be quite useful at reproducing basic galaxy scaling relations, and can be implemented and improved upon in simulations or SAMs in the future (Pandya et al. 2022).

What has not been extensively explored in these regulator models is the role of the CGM in regulating galaxy formation and the contribution of energy-loaded preventative feedback. Although Davé et al. (2012), for example, included a preventative feedback parameter that quantifies the amount of baryonic inflow from the IGM prevented from reaching the ISM, and thus remaining in the gaseous halo, the broad properties of cooling and heating in the CGM as its own reservoir are not explicitly tracked, leaving the CGM omitted on a phenomenological level. SAM models, which do explicitly include a halo gas reservoir, often assume that the thermal properties of the CGM are in equilibrium with those of their dark matter halos (White & Frenk 1991). There have been a few efforts to improve the cooling physics of halo gas in SAMs (Benson & Bower 2011; Lu et al. 2011; Cousin et al. 2015; Hou et al. 2018) and generate SAM predictions for the CGM that can be compared to observables (Faerman et al. 2022); however, such SAM models of galaxies and their CGMs lack an energetically self-consistent treatment of preventative feedback from galactic winds (Pandya et al. 2020).

While many basic properties of the CGM of the MW and external galaxies are still not well understood, observations have converged onto a general picture of the CGM as an

extended, multiphase reservoir composed of a hot phase ($T \sim 10^6$ K) directly measurable from X-ray emission, a warm-hot phase ($T \sim 10^{5-6}$ K) visible in UV absorption lines, a cold neutral and low-ion phase ($T \sim 10^4$ K), and a significant contribution of metals and dust (for reviews, see Putman et al. 2012 and Tumlinson et al. 2017). The CGM contains a substantial budget of baryons, and could play a major role in regulating galaxy evolution as it supplies fuel to the galaxy for star formation, but the galaxy in return shapes the CGM, as outflows driven by feedback processes alter the mass and energy content of the CGM. Thus, the properties of the CGM and galactic winds are deeply intertwined.

The aim of this work is to build on this understanding of the CGM as a regulator of galaxy evolution, and explore how different compositions of SNe-driven winds shape the properties of galaxies and their CGMs. In particular, we will track not only the flows of mass and metallicity of the CGM, but also the flows of energy, allowing for a self-consistent (albeit simplified) regulation of preventative feedback. We will show that the CGM is the natural seat of self-regulation in such models, with the key parameter shifting from the mass outflow rate to the energy outflow rate. Using our new model, we investigate whether we can match key observational scaling relations with reasonable assumptions about the energetics of galactic winds.

In the next section, we introduce the regulator model, along with the relevant equations governing mass evolution, the cooling efficiency of the CGM, followed by our treatment of preventative feedback from energy-loaded winds and metallicity evolution (Section 2). We then show the time evolution of a $10^{12} M_{\odot}$ halo and test our model over a range of halo masses, comparing its output to the stellar-to-halo mass relation and the ISM-to-stellar mass ratio, and its implications for the circumgalactic gas content (Section 3). We end our work with a discussion of its implications for self-regulation in galaxies and feedback, the connection to CGM-precipitation models, and a comparison to other regulator models (Section 4). We then summarize our conclusions (Section 5).

2. Gas-regulator Model

In this section, we introduce our one-dimensional regulator model, where the different components of the galaxy are each treated as reservoirs that exchange baryons at different rates. We consider a galaxy composed of seven reservoirs (see Figure 1): a dark matter halo (M_h), the stellar mass (M_*), the interstellar medium (M_{ISM}), the circumgalactic medium (M_{CGM}), the energy of the CGM (E_{CGM}), and the mass in metals of the CGM ($M_{Z,\text{CGM}}$) and of the ISM ($M_{Z,\text{ISM}}$). Note that, because we are focused on the CGM, we do not track the metallicity of the stars, and that a more detailed treatment of ISM metallicity beyond the illustrative one featured here would introduce additional free parameters that do not directly impact the evolution of the CGM.

We write down a simple set of ordinary differential equations for the evolution of these quantities based on some simple physical reasoning (including some free parameters), and solve for their evolution using a Runge–Kutta solver (using `solve_ivp` from the `scipy` python package). After introducing the basic equations that define the evolution of each of the mass reservoirs, we describe our treatment for the cooling rate for CGM gas and accretion, the lifting of CGM gas out of the halo through heating from energetic winds, and the metallicity enrichment of the CGM from SNe-driven outflows.

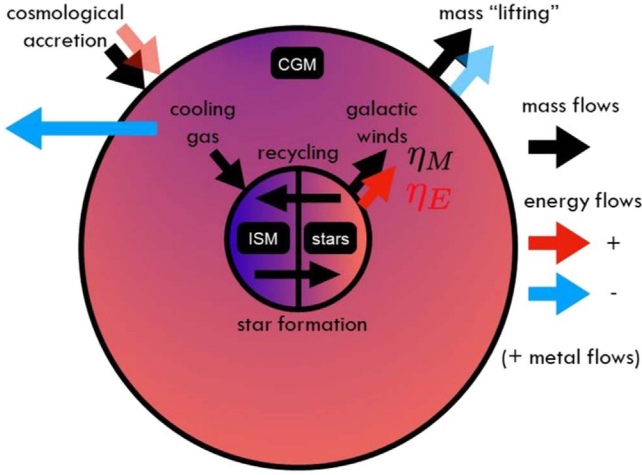


Figure 1. Schematic of one-dimensional regulator model. The baryonic components of the galaxy (the ISM, stellar mass, and the CGM) are distinct reservoirs, which exchange mass, energy, and metals. The black arrows represent the mass (and metal) flows, while the red/blue arrows symbolize the positive/negative flows of energy among the various components.

2.1. Structure of the Circumgalactic Medium

We begin by describing our simple model for the structure of the CGM. Our goal here is to write down a model that retains the basic properties but is analytic, or nearly so. We make two simplifying assumptions.

First, we take the halo to be isothermal, at temperature T_{CGM} , which is close to but not necessarily equal to the virial temperature, T_{vir} . The temperature we assume for the CGM is equal to $T_{\text{CGM}} = (\mu m_p / k) e_{\text{CGM}}$, where k is the Boltzmann constant and μ is the mean molecular weight, which we assume to be $\mu = 0.6$ in units of the proton mass. In fact, rather than the temperature we generally use the halo-specific energy, $e_{\text{CGM}} = E_{\text{CGM}} / M_{\text{CGM}}$, where E_{CGM} and M_{CGM} are the thermal energy and mass of the CGM, respectively.

In addition, we assume the mass density profile of the CGM follows a power law:

$$\rho(r) = \rho_0 \left(\frac{r}{r_0} \right)^{-\alpha}, \quad (1)$$

where $\alpha = 1.4$ so that the entropy profile goes as $K \propto T / \rho^{2/3} \sim r^{2/3}$ (Nelson et al. 2016; Fielding et al. 2020; Esmerian et al. 2021). As we will show, the basic behavior of the model is insensitive to reasonable variations in α . We note that we do not explicitly enforce hydrostatic equilibrium, nor is it expected due to the presence of heating and cooling flows (Stern et al. 2019, 2020); however, for $T_{\text{CGM}} \approx T_{\text{vir}}$, this profile is close to hydrostatic equilibrium for typical dark matter halo profiles.

These simple forms allow us to write down expressions for the mass of the CGM, which we take to range from $r_0 = 0.1 r_{\text{vir}}$ to r_{vir} :

$$\begin{aligned} M_{\text{CGM}} &= \int_{r_0}^{r_{\text{vir}}} \rho_0 \left(\frac{r}{r_0} \right)^{-\alpha} 4\pi r^2 dr \\ &= 4\pi \rho_0 r_0^3 \left(\frac{(r_{\text{vir}}/r_0)^{3-\alpha} - 1}{3-\alpha} \right), \end{aligned} \quad (2)$$

and similarly for the net radiative-cooling rate of the CGM gas:

$$\begin{aligned} \dot{E}_{\text{CGM, cool}} &= \int_{r_0}^{r_{\text{vir}}} \left(\frac{\rho}{\mu m_p} \right)^2 \Lambda(T_{\text{CGM}}, Z, z) 4\pi r^2 dr \\ &= 4\pi \rho_0^2 r_0^3 \left(\frac{\Lambda(T_{\text{CGM}}, Z, z)}{\mu^2 m_p^2} \right) \left(\frac{(r_{\text{vir}}/r_0)^{3-2\alpha} - 1}{3-2\alpha} \right). \end{aligned} \quad (3)$$

$\Lambda(T_{\text{CGM}}, Z, z)$ is the radiative-cooling rate, which we take from Wiersma et al. (2009), and depends on metallicity and redshift (due to a time-varying metagalactic radiation field), while the mean particle mass, μ , equals 0.6 in units of the proton mass (m_p). We note that the analytic forms fail when $\alpha = 3$ or $3/2$ (but the solution is well behaved, with the terms in parentheses becoming simply r_{vir}/r_0).

2.2. Mass Evolution

This section describes the evolutionary equations for the various mass reservoirs (halo, CGM, ISM, stellar) before turning to the CGM energy reservoir in the next section.

2.2.1. Halo Mass

We start with the overall evolution of the dark matter halo, M_{h} , which we assume to grow smoothly and monotonically with time, as given by a fit to numerical simulations from Dekel et al. (2009):

$$\dot{M}_{\text{halo}} = 0.47 M_{\text{halo}} \left(\frac{M_{\text{halo}}}{10^{12} M_{\odot}} \right)^{0.15} \left(\frac{1+z}{3} \right)^{2.25} \text{Gyr}^{-1}. \quad (4)$$

Since halos of the same mass can have different formation histories, it is important to note that Equation (4) defines the average halo growth rate for halos of a given mass.

2.2.2. Circumgalactic Medium Mass

We next turn to the evolution of the CGM mass component. Baryons enter the halo along with dark matter ($\dot{M}_{\text{CGM, in}}$), flowing first into the CGM before cooling and accreting into the ISM ($\dot{M}_{\text{CGM, cool}}$). In addition, star formation can directly eject ISM gas into the CGM ($\dot{M}_{\text{ISM, wind}}$) as well as providing energy that can heat the CGM, causing it to expand and “lift” gas out of the hot CGM and unbind it from the halo ($\dot{M}_{\text{CGM, out}}$). We write this schematically as

$$\dot{M}_{\text{CGM}} = \dot{M}_{\text{CGM, in}} - \dot{M}_{\text{CGM, cool}} + \dot{M}_{\text{ISM, wind}} - \dot{M}_{\text{CGM, out}}. \quad (5)$$

Each of these terms has relatively simple expressions and we discuss each in turn. To provide the first term, we assume that mass infalls from the IGM along with the dark matter:

$$\dot{M}_{\text{CGM, in}} = f_b f_{\text{prevent}} \dot{M}_{\text{halo}}, \quad (6)$$

where f_b is the cosmic baryon fraction and f_{prevent} is a halo-level preventive infall factor that we describe below, after discussing the CGM energy budget. Note that this differs somewhat from preventive feedback in traditional bathtub models (e.g., Davé et al. 2012) in that f_{prevent} is related to the accretion of gas from the IGM into the CGM, not directly to the ISM. In particular, our CGM energy model (described next) aims to explicitly calculate the traditional CGM preventive factor at the halo

scale, in addition to self-consistently accounting for the prevention of accretion to the ISM by extending the cooling timescale from the CGM.

The second term accounts for radiative energy losses of the CGM that allow some of the gas to cool to low temperatures (10^4 K or lower) and accrete onto the ISM. For this, we write simply

$$\dot{M}_{\text{CGM,cool}} = M_{\text{CGM}}/t_{\text{cool,eff}}, \quad (7)$$

where we define the effective cooling time, $t_{\text{cool,eff}}$, as the sum of the cooling time and the freefall at the virial radius. The second term accounts for the time the gas takes to accrete from the CGM into the ISM (this second term only becomes important at high redshift when the cooling times are short and the CGM fails to self-regulate):

$$t_{\text{cool,eff}} = \frac{E_{\text{CGM}}}{\dot{E}_{\text{CGM,cool}}} + t_{\text{ff}}. \quad (8)$$

The third term of Equation (5) accounts for mass ejected via a galactic wind due to star formation, which we parameterize with the usual mass-loading factor, η_M :

$$\dot{M}_{\text{ISM,wind}} = \eta_M \dot{M}_{\text{SFR}}. \quad (9)$$

Mass ejection (generally to a long-lived reservoir) is the primary mode of self-regulation in classical regulator models, but in our model mass ejected into the CGM can cool and accrete back to the ISM, as we will show. Instead, mass is lifted out of the CGM due to heating (from star formation and other energy sources). Heating of the CGM can cause overpressurization (i.e., $T_{\text{CGM}} > T_{\text{vir}}$), which lifts gas out of the halo into the IGM, where we assume it is unbound from the halo and does not return.⁵ We will shortly lay out the energy equation for the CGM; one term in that equation (Equation (18)) is $\dot{E}_{\text{CGM,out}}$, the rate at which energy flows out of the halo due to this overpressurization. We assume that this energetic outflow brings with it an equivalent amount of mass such that the outflowing gas has the same specific energy as the halo gas:

$$\dot{M}_{\text{CGM,out}} = \dot{E}_{\text{CGM,out}}/(E_{\text{CGM}}/M_{\text{CGM}}). \quad (10)$$

2.2.3. Interstellar Medium Mass

The ISM is fed from the CGM and loses mass to star formation and SN-driven winds. We express the evolution of the gas mass of the galaxy in the form

$$\dot{M}_{\text{ISM}} = \dot{M}_{\text{CGM,cool}} - (1 - f_{\text{rec}})\dot{M}_{\text{SFR}} - \dot{M}_{\text{ISM,wind}}, \quad (11)$$

where the first term describes gas accretion into the ISM from the CGM. The expression for $\dot{M}_{\text{CGM,cool}}$ is given in Equation (7). The next term describes the mass lost from the ISM due to star formation, and the mass returned to the ISM as stars recycle a fraction of their mass back to the ISM. We fix this instantaneous stellar recycling fraction to be $f_{\text{rec}} = 0.4$ (Kroupa 2001). The final term captures the mass lost from galactic winds, defined in Equation (9), and its efficiency is quantified in terms of the mass-loading factor η_M .

⁵ Gas that is uplifted out of the halo may cool and return to the halo on some timescale. The inclusion of this returning gas would require greater suppression of infall (smaller f_{prevent}) than we estimate in this work.

2.2.4. Stellar Mass

Considering next the stellar mass reservoir, the star formation rate, \dot{M}_{SFR} , is dictated by the gas mass of the ISM, M_{ISM} , and the timescale over which that gas mass is converted into stars:

$$\dot{M}_{\text{SFR}} = \frac{M_{\text{ISM}}}{t_{\text{dep}}}, \quad (12)$$

where t_{dep} is the depletion time. For simplicity, we do not distinguish between atomic and molecular gas and assume that all ISM gas participates in star formation. We use an estimate of the depletion time as a function of stellar mass derived from observations of the cold gas mass and star formation rates of low-surface-brightness and star-forming galaxies from McGaugh et al. (2017). We assume a redshift dependence of $(1+z)^{-3/2}$, similar to the Hubble timescale adopted in many previous regulator models, resulting in the depletion time we use for our model:⁶

$$t_{\text{dep}} = 10^{4.92} \left(\frac{M_{\star}}{M_{\odot}} \right)^{-0.37} (1+z)^{-3/2}. \quad (13)$$

We can express the full evolution of the stellar mass of the galaxy:

$$\dot{M}_{\star} = (1 - f_{\text{rec}}) \frac{M_{\text{ISM}}}{t_{\text{dep}}}, \quad (14)$$

when we consider the star formation rate and the fractional loss of stellar mass from mass recycled back to the ISM.

2.3. Circumgalactic Medium Energy Evolution

We turn next to the new feature of our model, an equation for the thermal energy of the CGM (we neglect here the kinetic energy component, which is explored in a companion paper by Pandya et al. 2022). As before, we account for all of the energy gain and loss terms for the evolution of E_{CGM} :

$$\dot{E}_{\text{CGM}} = \dot{E}_{\text{CGM,in}} - \dot{E}_{\text{CGM,cool}} + \dot{E}_{\text{ISM,wind}} - \dot{E}_{\text{CGM,out}}, \quad (15)$$

The first term represents the energy of infalling gas (Equation (6)), which we assume is associated with the specific energy of the halo:

$$\dot{E}_{\text{CGM,in}} = \left(\frac{kT_{\text{vir}}}{\mu m_p} \right) \dot{M}_{\text{CGM,in}}. \quad (16)$$

The second term of the energy evolution equation, representing radiative losses, is given in Equation (3). The third term is positive and comes from the energy associated with SN-powered galactic winds:

$$\dot{E}_{\text{ISM,wind}} = \eta_E \dot{M}_{\text{SFR}} \left(\frac{10^{51} \text{ erg}}{100 M_{\odot}} \right), \quad (17)$$

where we have parameterized the amount of SN-powered energy that escapes out of the ISM as η_E . As we will show, this is a key parameter that drives our CGM-regulated model.

⁶ Since the depletion times in low-mass systems are not well constrained observationally, we assume that for systems with $M_{\text{star}} < 5 \times 10^7 M_{\odot}$, below which the data become sparse, that the depletion time is constant and only involved with redshift and not with stellar mass.

Finally, the fourth term represents the energy that goes into lifting gas out of the CGM, unbinding it. We assume this only occurs if the CGM is overpressurized such that its specific energy exceeds the virial value. When this is true, we compute the outflow rate assuming that gas flows out at the hot gas sound speed, c_s :

$$\dot{E}_{\text{CGM,out}} = \max\left(E_{\text{CGM}} - \frac{kT_{\text{vir}}M_{\text{CGM}}}{\mu m_p}, 0\right) \left(\frac{c_s}{R_{\text{vir}}}\right). \quad (18)$$

This outflow of hot gas also drives a mass flux (see Equation (10)). The hot gas sound speed is the usual $c_s = (5kT_{\text{CGM}}/3(\mu m_p))^{1/2}$.

The inclusion of this mass and energy “lifting” term to the CGM describes the contribution from preventative feedback. By lifting a fraction of the CGM beyond the virial radius and (we assume) out of the gravitational clutches of the dark halo, feedback works to reduce the density of the CGM. This lengthens the radiative-cooling timescale, and thus regulates the rate of accretion out of the CGM onto the galaxy, and any subsequent star formation. The details of this “lifting” process are clearly complicated and the simple relation in Equation (18) is an approximation; however, small uncertainties in the proportionality can be accommodated by changing the effective energy-loading factor.

One of the last elements of the model is to define the halo-level preventative inflow factor, f_{prevent} , used in Equation (6). The idea here is that energy flowing out beyond the virial radius will heat IGM gas and prevent it from falling in. This effect has previously been found to be operating in FIRE simulations (Pandya et al. 2020). We take a deliberately simple form for this, defining it to be proportional to the ratio of the inflowing to outflowing energy. Although there is no strong physical justification for this particular form, it seems reasonable that this ratio of these energies should be a good measure of the importance of energetic outflows. In particular, we adopt⁷

$$f_{\text{prevent}} = \min\left(\alpha_{\text{prevent}} \frac{\dot{E}_{\text{CGM,in}}}{\dot{E}_{\text{CGM,out}}}, 1\right), \quad (19)$$

where we have defined a free parameter, which we take to be $\alpha_{\text{prevent}} = 2$, resulting in f_{prevent} values consistent with Pandya et al. (2020).

2.4. Metallicity of the Circumgalactic Medium

The significant share of metals observed in the CGM of galaxies is incontrovertible evidence for the presence of metals in galactic outflows (Prochaska et al. 2017). Metals in galactic winds arise in part by entrainment of previously enriched ISM gas and in part to the fact that SNe enrich the gas as it simultaneously injects energy and momentum. We parameterize the fraction of metals produced by SNe that wind up in outflows using the metal-loading factor, defined as $\eta_Z = \frac{\dot{M}_{Z,\text{out,SN}}}{\dot{M}_{Z,\text{SN}}}$. Note that this definition of η_Z includes only the metals in the wind directly enriched by SNe ejecta and not metals from the ISM that were entrained in the mass-loaded wind. This definition of the metal-loading factor means that if $\eta_Z = 1$, then all of the metals produced in SNe leave the galaxy in outflows. We also include the contribution of metals from entrained gas in the ISM, which we assume has a metallicity

equal to the metallicity of the ISM reservoir. Our model of CGM metal enrichment differs from Pandya et al. (2022), who do not distinguish between pure SNe ejecta versus entrained ISM material in outflows and instead assign a single metallicity to the wind, which for simplicity they take to be Z_{ISM} (this implicitly assumes heavily ISM-entrained winds).

If we include the metal mass of the CGM ($M_{Z,\text{CGM}}$) as its own reservoir, its evolution takes the form

$$\begin{aligned} \dot{M}_{Z,\text{CGM}} &= Z_{\text{IGM}}\dot{M}_{\text{CGM,in}} - Z_{\text{CGM}}\dot{M}_{\text{CGM,cool}} \\ &\quad + \eta_Z y_{\text{SN}}\dot{M}_{\text{SFR}} + Z_{\text{ISM}}\dot{M}_{\text{ISM,wind}} \\ &\quad - Z_{\text{CGM}}\dot{M}_{\text{CGM,out}}. \end{aligned} \quad (20)$$

The first term represents the accretion of metals from the IGM. We assume a constant metallicity for the IGM inflow of $Z_{\text{IGM}} = 0.01 Z_{\odot}$, where the IGM metallicity is (somewhat arbitrarily) assumed to be 1% of the solar metallicity $Z_{\odot} = 0.0134$ (Asplund et al. 2009). This is different from the usual assumption that the IGM metallicity is “pristine” and has only been enriched by Population III SNe. Here we imagine that some of the cosmic accretion has been further pre-enriched either by the galaxy’s own outflows or from galactic neighbors. The next term describes the loss of metals from the accretion of gas into the ISM, where $Z_{\text{CGM}} = M_{Z,\text{CGM}}/M_{\text{CGM}}$ represents the fraction of the CGM mass in metals. The third and fourth terms capture the direct enrichment of metals from SNe outflows and the metals gained from gas entrainment in the ISM, respectively. We assume the metal mass enrichment yield produced from one SN per 100 M_{\odot} is approximately equivalent to $y_{\text{SN}} \sim 0.033$ (consistent with a Kroupa 2001 initial mass function, where $(1 - f_{\text{rec}})y_{\text{SN}} \approx 0.02$), and $Z_{\text{ISM}} = M_{Z,\text{ISM}}/M_{\text{ISM}}$ describes the fraction of the ISM mass in metals. Lastly, the final term represents the metals that are lifted out of the halo, which we assume has the same metallicity as the CGM as a whole. We neglect forms of metal enrichment not directly tethered to SNe feedback, such as metal-enriched gas stripping from orbiting satellites, which are relatively less understood and remain areas of active debate.

2.5. Metallicity of the Interstellar Medium

The ISM is enriched with metals from SNe and from CGM gas accretion, while it loses metals to new star formation and SNe-driven winds out of the galaxy. Similar to the total ISM mass, we express the evolution of the ISM metallicity:

$$\begin{aligned} \dot{M}_{Z,\text{ISM}} &= Z_{\text{CGM}}\dot{M}_{\text{CGM,cool}} + (1 - \eta_Z)y_{\text{SN}}\dot{M}_{\text{SFR}} \\ &\quad - Z_{\text{ISM}}(1 - f_{\text{rec}})\dot{M}_{\text{SFR}} - Z_{\text{ISM}}\dot{M}_{\text{ISM,wind}}. \end{aligned} \quad (21)$$

The first term describes the metals gained by gas accretion from the CGM, which shares the metallicity of the CGM. Next, we include the enrichment of the ISM from the fraction of metals produced by SNe that do not leave the galaxy in winds, which is set by η_Z . The next term represents the metals lost to star formation and the mass in metals recycled back to the ISM (assuming that the stars and ISM have comparable metallicity and metals are only produced in SNe). The last term describes the metals lost in the entrained mass-loaded wind. The ISM metallicity as a function of halo mass and its dependence on different outflow parameters can be found in Appendix A.

⁷ Note that here $\dot{E}_{\text{CGM,in}}$ is defined as the energy of inflowing gas from the IGM at the full cosmic baryon fraction.

3. Results

Now that we have described our basic model, we explore it in detail for a single halo, before turning to the scaling relations that it predicts as the halo mass is varied.

3.1. Evolution for a $10^{12} M_{\odot}$ Halo

To get a sense of whether the regulator model can reproduce galaxy properties by the present day, we run our model on a MW-like galaxy. The top panel of Figure 2 shows the time evolution of the mass in each of our four mass reservoirs, for a $10^{12} M_{\odot}$ halo from a redshift of $z \simeq 6$ to the present day. The middle panel charts the evolution of the total CGM energy compared to its virial binding energy ($kT_{\text{vir}} M_{\text{CGM}}$). The bottom panel displays the CGM metallicity as a function of time with respect to solar metallicity. This run uses parameter values of $\eta_M = 0.1$, $\eta_E = 0.1$, and $\eta_Z = 0.2$, respectively, in line with typical values for the loading factors in MW-like galaxies seen in FIRE-2 (Pandya et al. 2021).

There is rapid growth in the CGM and ISM masses early on, as pristine gas from the IGM accretes onto the CGM before rapidly cooling and accreting onto the central galaxy. This prompts a steep initial rise in the gas mass of the galaxy, and this newly available fuel triggers star formation on a timescale of order t_{dep} . The birth of new stars increases the stellar mass, but their subsequent death through SNe begins to drive energy and mass outflows back into the CGM. Due to the relatively small mass-loading factor adopted here, the major contribution to the CGM is due to the energy loading, which heats the CGM and lifts mass out of the halo into the IGM. This loss of mass from the CGM not only serves as a counterbalance to the mass gains from early IGM accretion by limiting the mass of the CGM across a wide range of redshifts but also regulates the density of the CGM and therefore its overall cooling efficiency. This regulation of cooling limits the flow of gas into the ISM, resulting in generally slow growth of the ISM and stellar masses.

The model produces stellar and ISM masses on the order of $\sim 10^{10} M_{\odot}$, estimates that are slightly lower but broadly consistent with the total stellar mass of the MW of $\sim 5 \times 10^{10} M_{\odot}$ (Bland-Hawthorn & Gerhard 2016). The mass estimate of the CGM is also on order of $\sim 10^{10} M_{\odot}$, lying within the observational constraints of the CGM mass of the MW for reasonable choices of η_M and η_E (e.g., Salem et al. 2015; Tumlinson et al. 2017). However, we note that the total CGM mass is poorly constrained observationally.

The total energy of the CGM grows rapidly at early times from the infall of gas from the IGM. Radiative losses cause the gas to cool and accrete quickly into the ISM, where the early burst of star formation drives energy outflows back into the CGM. The energy loading of these outflows heats the CGM, raising its specific energy and limiting its cooling efficiency. Comparing the time evolution of the total energy of the CGM against its virial energy, we find that the total energy of the CGM exceeds its virial value, resulting in a CGM that is overpressurized. This overpressurization expands the CGM, lowering its density and lifting mass and energy beyond the virial radius. This process of heating the CGM and lifting gas out of the halo through overpressurization regulates the energy content of the CGM against radiative losses and energy gains from cosmic accretion and star formation, thus limiting the growth of the CGM energy to the present day.

The growth of M_{\star} produces metals, but after a steep climb over the first ~ 6 Gyr from SNe-driven outflows the growth of the CGM metallicity begins to flatten as it approaches the present day. Metal-rich outflows work to enhance future cooling from the CGM, while efficient energy loading works to reduce it. The metallicity of the CGM with respect to the solar metallicity approaches $Z_{\text{CGM}}/Z_{\odot} \simeq 0.18$ by $z = 0$, lower than existing estimates of the MW CGM's metallicity and similar hosts of $Z_{\text{CGM}} \sim 0.3 Z_{\odot}$ (Prochaska et al. 2017). This suggests that larger-metallicity outflows, reaccretion of metal-enriched gas from the IGM, or enrichment from other mechanisms not directly tethered to SNe feedback may be needed to match observations.

Our regulator model can produce galaxies by the present day with properties that are in qualitative agreement with observations of MW-like galaxies. This was achieved through mass outflows out of the ISM and energy regulation of the CGM acting as a mode of preventative feedback by constraining the total baryonic content of the galaxy.

3.2. Galaxy Scaling Relations

Next, we compare the $z = 0$ galaxy properties predicted from our model to galaxy scaling relations in the range $M_h = 10^{10} - 10^{12} M_{\odot}$. SNe are believed to drive the primary mode of feedback and star formation self-regulation for galaxies in halos below $\sim 10^{12} M_{\odot}$, so the regulator model should be compared in this range. Since the effects of AGN-driven feedback are not considered in this work, disparities at the high-mass end of the considered range may be present between the data and the model.

3.2.1. $M_{\star}/M_h - M_h$ Relation

We display the predicted $M_{\star}/M_h - M_h$ relation over this range for a set of different outflow parameters in Figure 3, plotted alongside the estimated observed stellar masses with uncertainties and their derived halo mass from abundance matching from Behroozi et al. (2019). The relation rises as a power law until peaking at a mass of $10^{12} M_{\odot}$, where the stellar mass fraction is largest, and then steadily falls for more massive halos as the quenching effects of AGNs take hold. We choose an initial set of outflow parameters, setting $\eta_M = 1$, $\eta_E = 0.3$, and $\eta_Z = 0.5$. In our exploration, we modulate the strength of one outflow parameter at a time, while keeping the values of the other two set to their fiducial values.

As the left panel demonstrates, the predicted stellar mass for low-mass halos is remarkably robust against changes in η_M , as the mass-loading factor is increased by a factor of 200. The only significant impact is to reduce the stellar mass of the highest-mass halos when using very highly mass-loaded winds. This suggests that the system self-regulates to similar galactic properties despite large changes in η_M . Self-regulation in this instance means that enhancements in the mass loading of outflows increase the mass and density of the CGM, which increases the CGM's ability to cool and accrete gas back to the galaxy. When η_E is held constant, highly mass-loaded outflows also lower the specific energy of the CGM. This lowers the overpressurization of the CGM and thus the flux of mass and energy leaving the halo, resulting in a larger f_{prevent} factor at the virial radius. Both of these processes—weakening the suppression of mass infall from the IGM and enhancing radiative losses of CGM gas—restrict the ability of mass-loaded

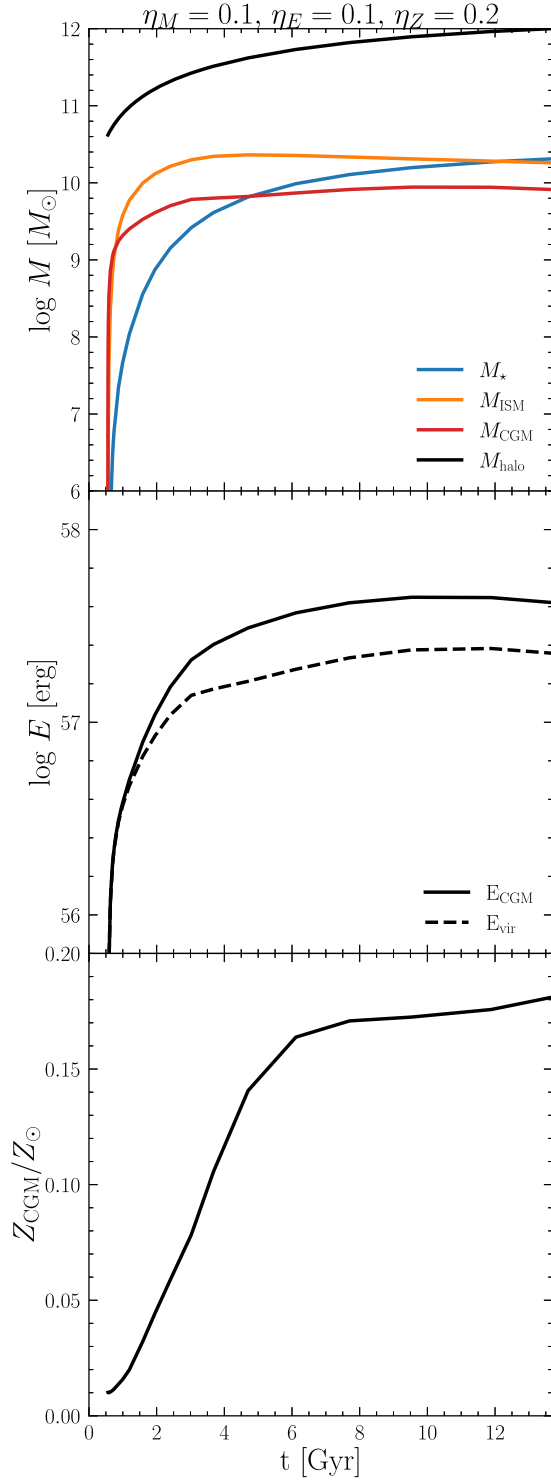


Figure 2. Time evolution of the mass of each reservoir in the regulator model (upper), the total energy of the CGM (solid) compared to its virial binding energy (dashed, middle), and the metallicity of gas in the CGM with respect to the solar metallicity (lower) for a $10^{12} M_{\odot}$ mass halo from $z \simeq 6$ to $z \simeq 0$. The mass, energy, and metal loadings are equal to $\eta_M = 0.1$, $\eta_E = 0.1$, and $\eta_Z = 0.2$, respectively.

outflows to meaningfully reduce the present-day stellar mass of galaxies on their own.

The largest η_M values explored in Figure 3 do appear to be slightly more effective at reducing the overall stellar mass in more massive halos, which may seem counterintuitive, but this

occurs only when the assumed feedback parameters fail to overpressurize the CGM. The M_*/M_h ratio flattens at halo masses beyond a threshold mass, which becomes lower as η_M increases. This occurs when η_M is large enough at a given halo mass (and given η_E) such that the outflow specific energy (and so e_{CGM}) drops below $kT_{\text{vir}}/(\mu m_p)$, meaning that the CGM is no longer overpressurized. This shuts off all energy and mass outflows at the virial radius (Equation (18)) and, with that, any preventative feedback at the halo scale ($f_{\text{prevent}} = 1$). The impact of larger values of η_M on the stellar mass beyond that threshold are still countered by enhancing CGM density and cooling, but are no longer affected by any cosmic outflows.

The center panel of Figure 3 displays the influence of changing η_E . Increasing the energy-loading factor of the outflows has the most significant impact of all outflow parameters, reducing M_* for larger η_E . Increasing η_E has the effect of enhancing the mass and energy lifted out of the CGM, as well as heating a larger share of IGM gas beyond R_{vir} and preventing its accretion. This reduces the CGM mass and density, and thus its ability to cool. Lowering the accretion rate reduces the overall star formation rate, resulting in much lower estimates of the present-day stellar mass for all halos. Since the mass lifted out of the halo is assumed to never return to the galaxy in our model, increasing η_E has the effect of permanently removing baryons from the galactic system. It is also worth noting that the model is able to produce stellar masses in the lowest-mass galaxies approaching those of observations with $\eta_E \sim 1$. This is despite having $\eta_M = 1$, which is at least an order of magnitude smaller than what is usually required to match galaxy scaling relations at the low-mass end. Interestingly, plotting the $M_*/M_h - M_h$ relation from the regulator model for different constant values of η_E against the observed relation reveals that in order to reproduce the halo mass dependence of the observed relation, η_E must depend on halo mass, favoring η_E close to unity for the lowest-mass halos and ~ 0.1 for MW-like halos.

As for changing η_Z (rightmost plot), we find only a very small effect on the stellar mass of the galaxy in the halo mass range explored. Increasing the metallicity of the winds increases the overall cooling efficiency of the CGM. However, because of the tight energy regulation, this enhanced cooling does not result in a significantly larger stellar mass (the mean density of the CGM is decreased by feedback to counterbalance the enhanced metallicity, resulting in nearly the same total cooling and star formation). The cancellation is such that this parameter appears to only make a meaningful difference in the accretion rate in halos with high star formation (and more massive halos).

The outflow parameter with the most significant influence on the present-day stellar mass is η_E , likely pointing to its prominent role in regulating the density of the CGM and limiting future gas cooling through preventative feedback. This form of preventative feedback becomes increasingly important in lower-mass halos. We will parameterize and discuss this dependence between η_E and M_h in Section 3.3.

3.2.2. $M_{\text{ISM}}/M_* - M_*$ Relation

Now we turn to the relation between the ISM gas and the stellar mass, which encodes star formation efficiency and can be constraining on models of galaxy evolution. Figure 4 compares the best-fit single power-law fit for the total cold gas mass as a function of M_* over the range $7.3 \lesssim \log(M_*/M_{\text{halo}}) \lesssim 11.2$ for

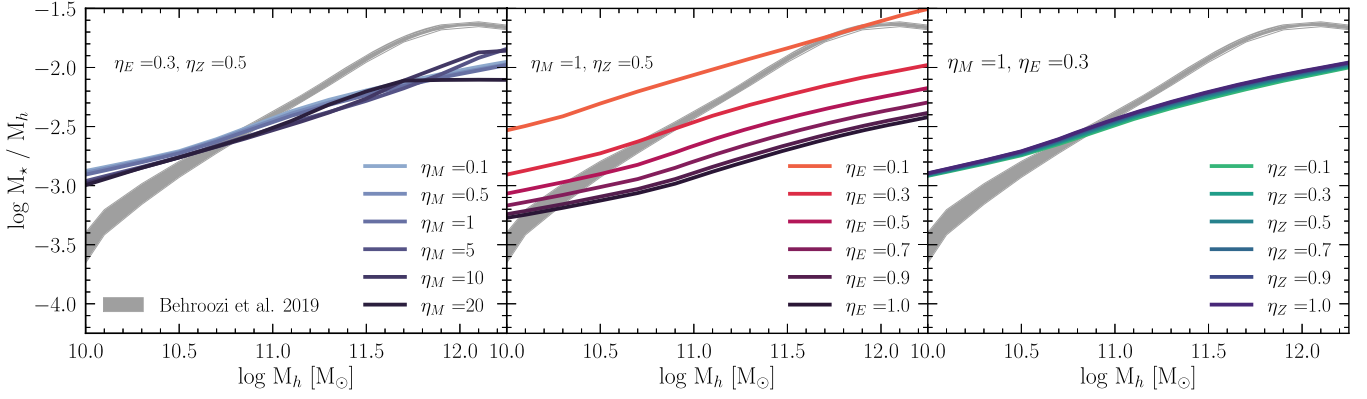


Figure 3. Log of M_*/M_h from the regulator model as a function of halo mass, compared to the median observed stellar mass with uncertainties in gray and their derived halo mass from abundance matching from Behroozi et al. (2019). Estimates of M_*/M_h are presented as a function of wind mass loading η_M (left), energy loading η_E (middle), and metal loading η_Z (right). The annotations of each plot display which parameters were kept constant in the iterations of the model on display.

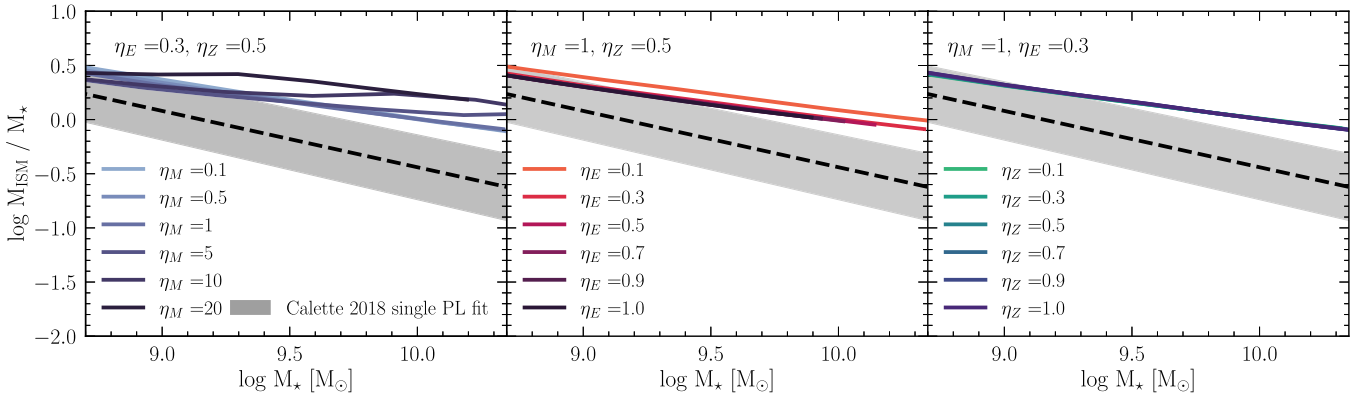


Figure 4. Log of M_{ISM}/M_* from the regulator model as a function of stellar mass, compared to the best-fit single power-law fit for the total cold gas mass as a function of M_* over the range $7.3 \lesssim \log(M_*/M_h) \lesssim 11.2$ for late-type galaxies from Calette et al. (2018). Estimates of M_{ISM}/M_* are presented as a function of wind mass loading η_M (left), energy loading η_E (middle), and metal loading η_Z (right). The annotations of each plot display which parameters were kept constant in the iterations of the model on display.

late-type galaxies from Calette et al. (2018) to the gas-to-stellar mass relation at $z = 0$ for the regulator model.

Figure 4 shows the $M_{\text{ISM}}/M_* - M_*$ relation as a function of outflow parameters. Changes in the energy (middle panel) and metallicity (right panel) composition of the outflows makes negligible difference to the proportion of gas mass to stellar mass over the parameter and halo range studied. The mass-loading factor (left panel) makes the most discernible difference in the $M_{\text{ISM}}/M_* - M_*$ relation, where more efficient mass loadings somewhat increase the ratio of gas mass to stellar mass for all galaxies and leads to a flatter dependence with stellar mass. The larger mass loading lowers the specific energy of the CGM and inhibits the suppression of cosmic inflow (larger f_{prevent} means more gas falls in), especially in more massive halos. This results in a more massive CGM and inevitably a more massive ISM reservoir due to the prompt radiative losses of the halo gas.

Our current treatment of the star formation produces a shallower gradient with increasing stellar mass than the observed power-law fit in Calette et al. (2018). This means that we predict an excess of gas with increasing halo mass. Although this could stem from a sampling bias in the data where we derive our depletion time, or from uncertainties in H I or molecular gas content, the size of the mismatch seems significant. However, as we discuss in Appendix B, the slope and amplitude of this relation in our model depends greatly on our choice of the depletion time. This dependence makes sense

because the depletion timescale governs the rate at which gas in the ISM is converted to stars. Additional feedback from AGNs may also help to ameliorate these conflicts at the higher-mass end, providing another means of reducing the ISM mass and quenching star formation. As demonstrated, we are able to vary the depletion time to match this relation and are still able to produce galaxies with stellar masses in qualitative agreement with observational constraints.

3.2.3. Implications for the Circumgalactic Medium Gas Content

The properties of the CGM and the properties of galactic outflows are intertwined, such that changes to the composition of galactic winds ought to greatly influence the properties of the CGM. Figure 5 plots the mass (upper panel) and metallicity of the CGM (lower panel) as a function of halo mass for different wind-loading factors. Broadly, we find that the CGM mass at a given halo mass is mostly dependent on the mass loading while less sensitive to the adopted energy-loading factor (in contrast to what was seen for the stellar mass–halo mass relation), and that the metallicity drops as η_M or η_E increases, while it (unsurprisingly) increases with increasing η_Z . In the following paragraphs, we examine these trends more carefully.

First, we see with the leftmost panels of Figure 5 that increasing η_M has the fairly predictable effect of increasing the overall CGM mass (although not linearly with η_M). This is true for all halo masses in our range. Since we include the metals in

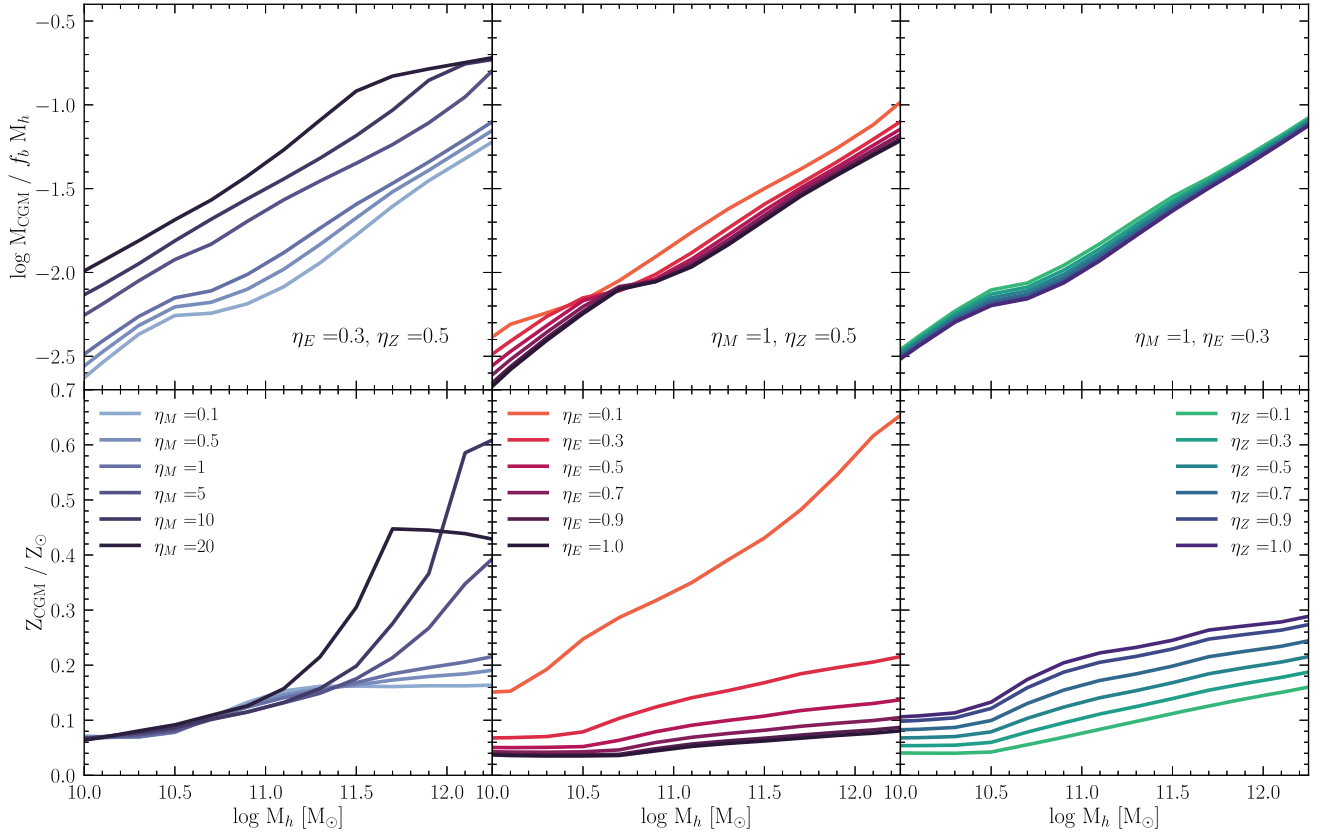


Figure 5. Estimates of $\log(M_{\text{CGM}}/f_b M_h)$ and the CGM metallicity with respect to the solar metallicity from the regulator model as a function of halo mass. Estimates of M_{CGM}/M_h and Z_{CGM}/Z_\odot are presented as a function of wind mass loading η_M (left column), energy loading η_E (middle column), and metal loading η_Z (right column). The annotations of each plot display which parameters were kept constant in the iterations of the model on display on a column.

the entrained ISM gas, we would expect that increasing the mass loading should also enhance the overall metallicity of the CGM. However, this expected relationship becomes more complicated when the CGM is overpressurized. The combination of mass and metals recycling back to the galaxy, and weaker preventative feedback allowing more accretion of metal-poor gas from the IGM, work to regulate the CGM metallicity when adjusting the mass loading. When the CGM is not overpressurized, as we see in the more massive halos with the largest assumed values for η_M , the mass-loaded outflows are more successful at launching metals from the ISM into the CGM.

Exploring the variation of the energy loading in the middle column, we see that more efficient energy loading has the opposite effect, reducing the overall mass of the CGM as energetic flows from SNe heat the CGM and lift gas and metals out of the halo. The reduction of star formation in the high- η_E scenario also stymies overall metal production in the galaxy, leaving less to be ejected into the CGM in the first place. The CGMs of the lowest-mass halos are quite metal-poor, peaking around $\sim 15\%$ of solar metallicity when $\eta_E = 0.1$ before getting progressively smaller as energy loading is increased, approaching metallicities by the present day that are not much higher than what we assumed for the background metallicity of the IGM of $Z_{\text{IGM}}/Z_\odot = 0.01$. This is consistent with the interpretation that dwarfs easily lose most of the metals that their stars produced in outflows to the IGM (Muratov et al. 2017; Pandya et al. 2021).

Increasing η_Z has a weak impact on the CGM mass but a strong influence on the metallicity: the metallicity of the CGM

can reach values of $\sim 30\%$ of solar metallicity in MW-mass halos when $\eta_Z = 1$, but a large η_Z alone from direct enrichment from SNe does not seem as effective at raising the CGM metallicity as decreasing energy loading or increasing the mass entrained in galactic winds. Large η_Z still leaves the CGM metallicity around 10% of the solar metallicity in the lowest-mass halos of our range. When considering the mass, metal-enriched winds do have the effect of increasing the cooling efficiency in the CGM, leading to more mass lost via cooling and accretion in the galaxy. However, this mass loss from an increase in cooling efficiency is small relative to the changes in the CGM mass that occur when you vary η_M or η_E .

The CGM mass estimates for MW-mass galaxies in Figure 5 are lower than those of the models presented in Faerman et al. (2020, 2022), where they find MW CGM mass estimates in the range of $\sim 3\text{--}10 \times 10^{10} M_\odot$. These models have been shown to agree with a broad variety of observational constraints on the MW’s CGM. However, our CGM masses can approach those of Faerman et al. (2020, 2022) when η_E is lower than ~ 0.1 . The CGM masses of the lowest-mass halos in Figure 5 disagree with the values found in FIRE-2 simulations (Pandya et al. 2020). CGM masses at the low-mass end are sensitive to not only the mass loading, which in FIRE is at least a factor of 2 higher (and even more so at higher redshift) than our maximum assumed $\eta_M = 20$, but also the shape of the cooling curve. The lowest CGM masses are found in dwarfs where the CGM temperature approaches the peak of the cooling curve.

Since we assume an isothermal CGM with temperature derived from the specific energy, we cannot model the variations in gas phases captured by observations, but our

work does have important implications for the CGM’s multiphase structure. Gas that cools and precipitates out of a hot halo onto the galaxy will be transitioning to cooler, more dense gas phases, forming structures that could resemble the high-velocity cool cloud complexes observed in the MW’s CGM (Maller & Bullock 2004; Fraternali et al. 2015; Li & Tonnesen 2020). On the hotter end, energetic outflows could heat gas from cool to warm phases (preventing its accretion) as well as heat warmer gas to supersonic temperatures before it ultimately becomes unbound from the halo (Das et al. 2021).

3.3. The Halo-mass Dependence of Wind Energy Loading

Comparisons of the regulator model with the M_*/M_h - M_h relation in Figure 3 indicate that η_E must depend strongly on halo mass. To ascertain the form of this dependence, we perform a recursive bisection using `optimize.bisect` from the `scipy` python package to find the optimal value of η_E that would yield the closest agreement between the model and the M_*/M_h - M_h relation at $z=0$ from Behroozi et al. (2019).

Previous work on stellar feedback in low-mass galaxies from simulations and observations has found that mass loadings likely depend on halo mass (see the recent review by Collins & Read 2022). For our recursive bisection on η_E , we assume that the mass-loading factor of outflows has a simple power-law dependence with halo mass with the form

$$\eta_M = \left(\frac{M_{\text{halo}}(z=0)}{10^{12} M_\odot} \right)^{-\beta}, \quad (22)$$

where β is a power-law index, which we set to $\beta=0.5$. This value of β translates to larger mass loadings for lower-mass halos, where $\eta_M=10$ and $\eta_M=1$ for halos of mass $\sim 10^{10} M_\odot$ and $\sim 10^{12} M_\odot$, respectively. We assume this scaling for β such that our values for η_M are comparable to those derived from observations of galactic winds in nearby dwarf and MW-like galaxies (Chisholm et al. 2017; McQuinn et al. 2019). We also assume $\eta_Z=0.5$, the same as in Section 3.1. Metal loading may also scale with halo mass in real galaxies, but, as we demonstrated in Section 3.2.1, our results for the stellar-to-halo mass relation are not strongly dependent on our choices for η_M and η_Z , and should not significantly alter our fitted value for η_E .

We plot the optimal values of η_E from our recursive bisection to match the median stellar mass at a given halo mass at $z=0$ in the top panel of Figure 6, along with a best-fit power-law relation of η_E as a function of halo mass using `optimize.curve_fit`. This power-law relation takes the form

$$\eta_E = A \left(\frac{M_{\text{halo}}(z=0)}{10^{12} M_\odot} \right)^{-\lambda}, \quad (23)$$

and finds good agreement with fitted parameter values of $A=0.065 \pm 0.009$ and $\lambda=0.60 \pm 0.04$. We find that our model prefers $\eta_E \sim 1$ for the lowest-mass halos and ~ 0.1 for MW-mass halos.

Our best-fit model also yields an estimate for the total CGM preventative inflow factor, f_{prevent} , as a function of halo mass. Displayed in the middle panel of Figure 6, we find that mass and energy outflows from the halo suppresses cosmic inflow to well below the cosmic baryon fraction, reaching $f_{\text{prevent}} \sim 0.3$

in the lowest-mass halos. Preventative inflow factors of $f_{\text{prevent}} \sim 0.3$ are also found in FIRE simulations for similarly low-mass halos (Pandya et al. 2020), and rise to $f_{\text{prevent}} \sim 1$ for MW-mass halos, slightly higher than the results of our model where $f_{\text{prevent}} \sim 0.8$ in similar systems. In the bottom panel, we show the resulting model stellar mass as a function of halo mass and its agreement with the Behroozi et al. (2019) relation.

The relation we find, in which η_E decreases in more massive halos, appears consistent with the results of FIRE-2 simulations, which also find larger energy loadings in low-mass dwarfs relative to MW-like halos at both high and low redshifts (Pandya et al. 2021). This result may conflict with results from “tall-box” simulations like TIGRESS, which show a flat relationship between η_E and star formation density and lower values of η_E overall ($\eta_E \sim 0.1$; Li & Bryan 2020). These ISM patch simulations were done under MW-like conditions with solar metallicities (Kim et al. 2020). High-resolution simulations that can probe the interaction between SNe and the ISM under low-metallicity conditions will be needed to better constrain η_E in low-mass galaxies.

4. Discussion

4.1. How the Model Self-regulates

The insensitivity we see to varying the mass-loading factor of galactic outflows suggests that the model is self-regulated to a significant extent, by which we mean that changes to the composition of outflows prompts a change in the cooling efficiency of the CGM, which in turn shapes the properties of the galaxy through regulating future gas accretion. Increasing η_M serves to enhance future accretion by increasing the density of circumgalactic gas, shortening the cooling timescale and enabling the rapid precipitation of gas back into the ISM in short order. The timescale of this reaccrion of gas in real galaxies is not well understood, but likely could persist for multiple cycles, providing a significant source of gas accretion to galaxies at low redshift (Oppenheimer et al. 2010; Ford et al. 2014; Anglés-Alcázar et al. 2017).

This form of self-regulation is not the case for η_E . Instead, increasing η_E enhances the heating of the CGM for a given amount of star formation, allowing more mass to be lifted out of the CGM and increasing t_{cool} . What makes the model so sensitive to the energy loading of the winds is its ability to remove baryons from the halo entirely, while adjusting η_M or η_Z only serves to shift baryons to a different component of the galaxy for a short while before they return back to the galaxy. We note that in real galaxies material unbound from the halo by energy-driven winds may eventually cool and return back to the halo on some (potentially long) timescale. Building a better understanding of both the timescales of recycled gas from outflows and the return of gas that has been expelled beyond the viral radius is required to better link observed galaxy scaling relations and the properties of SNe-driven winds.

To understand how this self-regulation works in detail, we examine Figure 7, which shows the energy and mass flows in three halos spanning the mass range of interest (with $10^{10} M_\odot$, $10^{11} M_\odot$, and $10^{12} M_\odot$ in the left, center, and right columns, respectively). In each case there is an initial period of adjustment between rapid cooling and heating by early star formation while the system comes into a quasi-equilibrium (on a timescale dictated by the depletion time) and then a generally slow evolution of both the energy and mass flows over time,

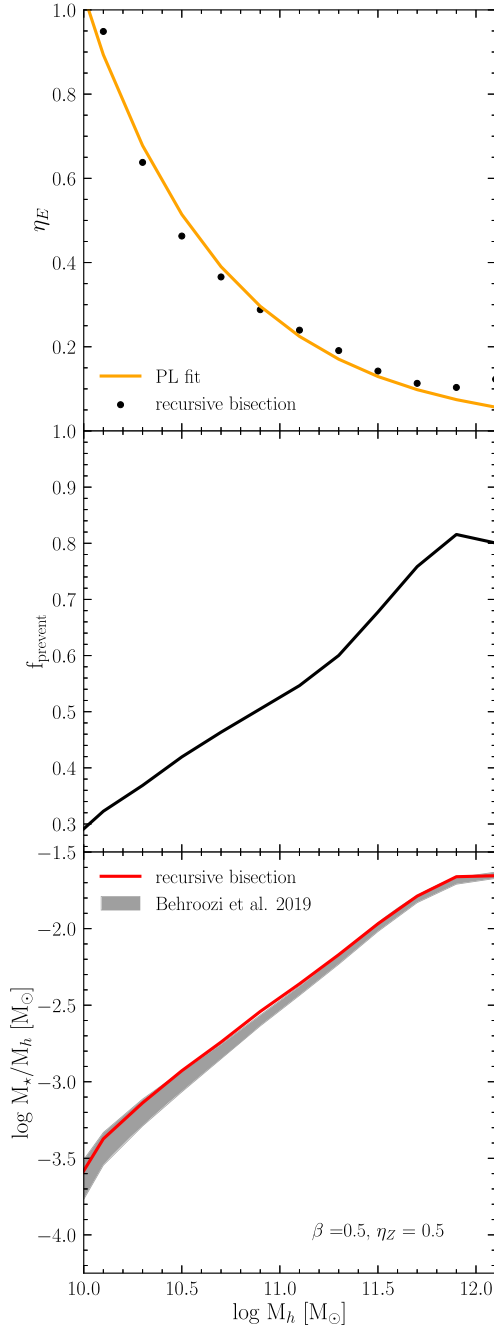


Figure 6. Energy loading η_E as a function of halo mass from recursive bisection (points) plotted with its best-fit power-law fit (orange, top). The middle shows the preventative inflow factor f_{prevent} as a function of halo mass for the optimal choice of η_E . Log of M_*/M_h from the regulator model computed with η_E from recursive bisection as a function of halo mass, compared to the median observed stellar mass with uncertainties in gray and their derived halo mass from abundance matching from Behroozi et al. (2019) (bottom). The annotations on the bottom plot display which parameters were kept constant.

with the evolution timescale set mostly by changes in the accretion rate (i.e., on a Hubble time). For the two lower-mass halos, equilibrium is largely dictated by a balance between the energetic input from SNe and the energy required to lift mass out of the CGM. Indeed, from the close balance of the cosmic inflow and CGM outflow terms in the \dot{M}_{CGM} curves (second row of panels), we see that the star formation rate is being set by the requirement that the CGM mass be held roughly constant (so that its cooling rate provides just enough mass to

power the star formation). This simple balance of two terms is more complicated in the highest-mass ($10^{12} M_\odot$) halo as the energy provided by the inflowing gas starts to become important (this is driven by the fact that the specific energy of the inflowing gas scales as $M^{2/3}$); however, the self-regulated quasi-equilibrium behavior still holds.

The result of this self-regulation can be seen in the bottom two rows. The mass builds up relatively slowly and energetic preventative feedback is working on two levels: regulating the CGM mass but also preventing the inflow of gas from the IGM. We note that the details of this evolution depend somewhat on the redshift evolution of the depletion time, which is not well constrained at high redshift (particularly for low-mass halos). Our default selection is a relatively rapid evolution of t_{dep} such that the star formation is high at high redshift and the ISM mass is kept low; a more gradual evolution results in a slower build up of the stellar component and a high ISM mass at high redshift. However, the overall self-regulatory behavior is robust to changes in the depletion time, with the exception that longer depletion times at early times cause a longer period of oscillatory self-adjustment and, in extreme cases, can cause a large fraction of the overall gas accretion into the ISM to occur at early times, particularly for low-mass halos.

4.2. Importance of Preventative Feedback Compared to Ejective Feedback

The leftmost panel of Figure 8 displays what happens to the $M_*/M_h - M_h$ relation when we remove all feedback, setting η_M , η_E , and η_Z equal to zero. We recover the classical result from early galaxy formation models of overcooling of baryons into the center of the dark matter halo and the overabundant production of stars (White & Rees 1978; Dekel & Silk 1986; White & Frenk 1991).

Removing gas from the galaxy through galactic outflows with high-mass-loaded winds has been a key part of most previous solutions to this problem (e.g., Kereš et al. 2009). To demonstrate that we can recover this result, that ejective feedback ($\eta_M > 0$) alone is capable of addressing the problems of overcooling, we set $\eta_E = 0$, removing the primary source of preventative feedback within the regulator model. We explore two instances where $\eta_E = 0$: one where all mass ejected from the central galaxy is deposited into the CGM and remains within the circulation of baryon flows (middle), and the extreme (but traditional) scenario where SNe-driven outflows launch all their gas out of the ISM such that it escapes to the IGM (right).

When ejected gas is deposited into the CGM with our simple power-law dependence of η_M with halo mass, mass loadings in low-mass galaxies only begin to touch the Behroozi et al. (2019) constraints when β approaches 1.3. This occurs because more efficient mass loading is able to slightly reduce the stellar mass, but in the absence of a means to remove baryons from the halo most gas recently ejected from the galaxy accretes back to the ISM in short order and provides fuel for star formation. In the scenario where gas is driven directly out of the galaxy and does not return, we can significantly reduce the stellar mass, but large values for β in Equation (22) are required to drive down the stellar mass such that it agrees with observed galaxies. However, this requires mass loadings as high as $\eta_M \sim 100$ in the lowest-mass halo explored by our model, which is similar to values in previous cosmological simulations and SAMs (e.g., Muratov et al. 2015;

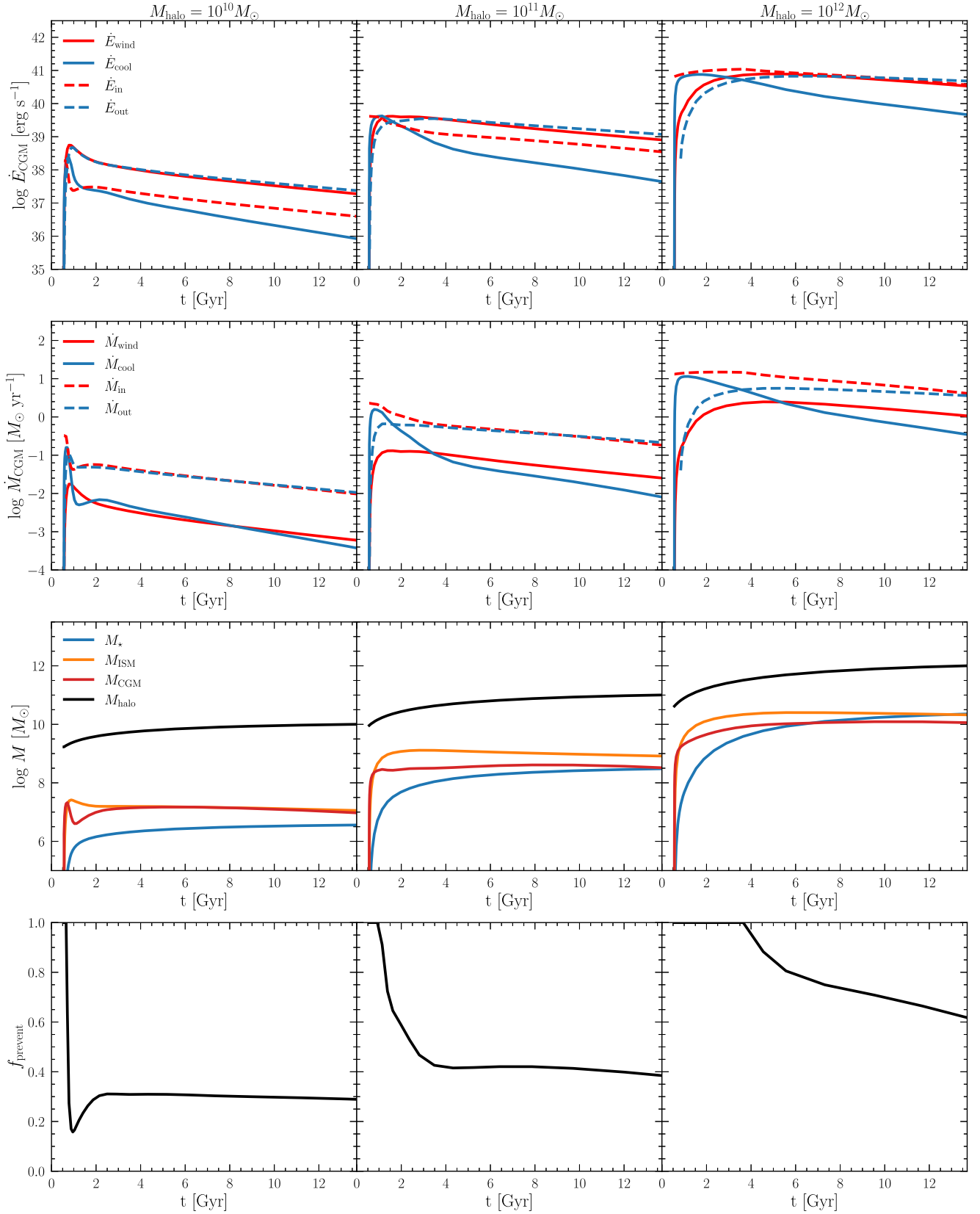


Figure 7. Time evolution of the logarithmic values of the flows in energy (topmost row) measured in ergs Gyr^{-1} and mass flows (top middle row) in $M_{\odot} \text{ Gyr}^{-1}$ for each sink and source term for the CGM reservoir in halos of mass $M_{\text{h}} = 10^{10} M_{\odot}$ (left), $10^{11} M_{\odot}$ (center), and $10^{12} M_{\odot}$ (right), respectively. Positive source terms are colored red while negative sink terms are in blue. Solid lines distinguish mass and energy flows at the galaxy–CGM interface, while dashed lines represent flows across the boundary of the CGM and IGM. The bottom middle row tracks the time evolution of the mass of each reservoir in the regulator model, and the bottom row tracks the evolution of the preventative inflow parameter f_{prevent} for each halo mass to the present day.

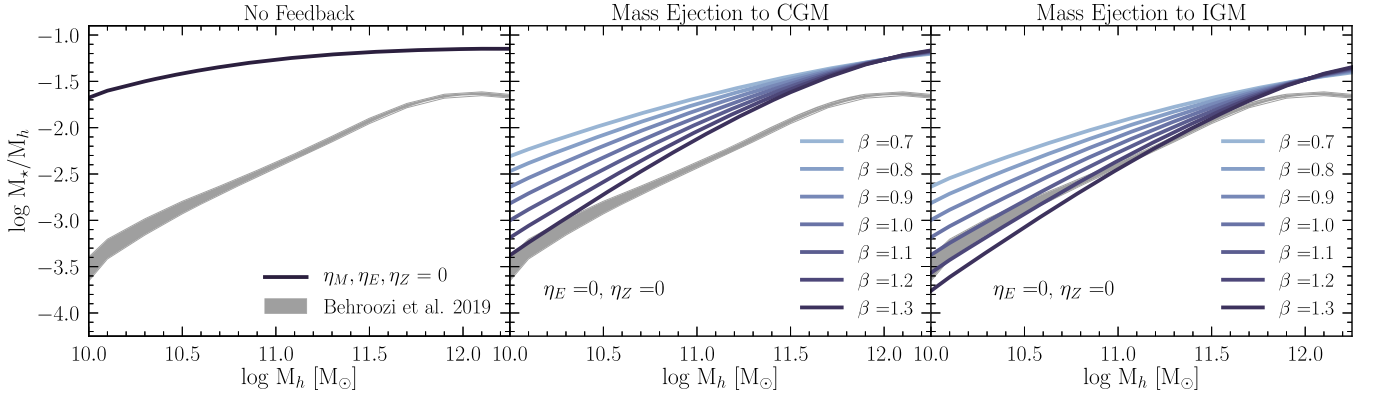


Figure 8. Log of M_*/M_h from the regulator model as a function of halo mass compared to the median observed stellar mass, with uncertainties in gray and their derived halo mass from abundance matching from Behroozi et al. (2019). The left plot shows the estimates of the log of M_*/M_h in the “No Feedback” case, where $\eta_M = \eta_E = \eta_Z = 0$. The middle and right plots show the same relation, but in the altered scenarios where winds of increasing mass loading eject all of their mass to the CGM or mass is ejected directly to the IGM, respectively, while $\eta_E = 0$. The annotations of each plot display which parameters were kept constant in the iterations of the model on display.

Anglés-Alcázar et al. 2017; Pillepich et al. 2018; Nelson et al. 2019; Pandya et al. 2020, 2021).

The difference between the two scenarios in the middle and right panels of Figure 8, SNe-driven winds ejecting gas into the CGM or ejecting all of the gas into the IGM, demonstrate the prominent role of the CGM in regulating the baryonic content of galaxies through cooling and accretion. High-specific-energy feedback provides a means of preventing further accretion by heating the gas and supplying additional thermal support against radiative losses, suppressing cosmic infall from the IGM and lifting heated gas out of the halo.

4.3. Connection to Precipitation: the $t_{\text{cool}}/t_{\text{ff}}-M_h$ Relation

There has been considerable evidence from observations and simulations of the intracluster medium (ICM) that precipitation-regulated feedback from a central heating mechanism of the cluster suspends the ICM gas in a state of critical balance, with the ratio of the cooling time to the freefall time $\gtrsim 10$ in massive galaxies (for a recent review, see Donahue & Voit 2022). Gas in the ICM becomes increasingly susceptible to condensation as the ratio falls below this precipitation limit. When this occurs, the condensing gas will fuel accretion onto the cluster’s central black hole, and the resulting energetic feedback from the black hole (in the form of a jet) will heat the gas and lengthen the cooling timescale of the gas, bringing the circumgalactic gas back to equilibrium such that the ratio exceeds 10. In clusters this process is thought to be the primary mechanism that keeps the galaxy quenched and the ICM regulated.

This same mechanism has been suggested to be operating in galaxies, with the ICM replaced by the CGM and SNe playing the role of the central black hole (Voit et al. 2015a). Fielding et al. (2017) showed this mechanism could be at play in the CGM when η_E/η_M is sufficiently high. The model we describe in this paper is similar in many respects but is not directly connected to precipitation (although that is a natural manifestation of our CGM cooling). In this section, we explore the connection to see if the CGM properties we find can be matched on to this critical balance picture.

The cooling time extends to longer timescales as the density drops farther out in the halo, while the freefall time of the gas also increases with distance (generally more slowly), giving the ratio a slowly rising radial profile. For Figure 9, we choose to

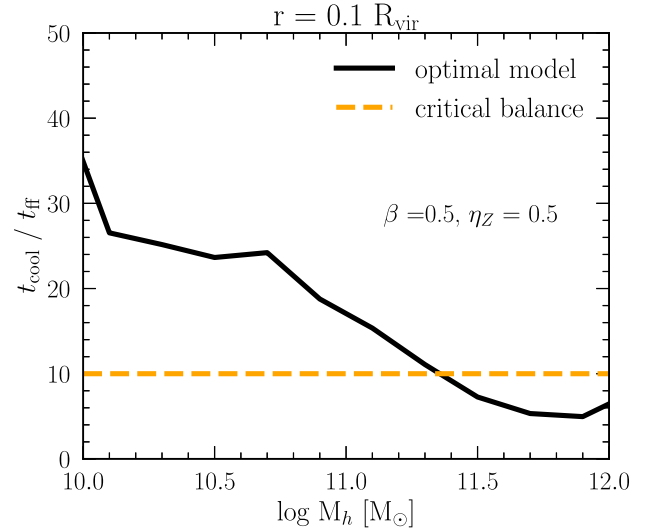


Figure 9. The ratio of the cooling time to the freefall time, $t_{\text{cool}}/t_{\text{ff}}$, evaluated at $R = 0.1 R_{\text{vir}}$ as a function of halo mass with the optimal choice of η_E from recursive bisection. The annotations on the bottom plot display which parameters were kept constant. The orange dashed line marks the critical balance, the predicted $t_{\text{cool}}/t_{\text{ff}} \gtrsim 10$ of gas in precipitation models of the CGM.

evaluate the $t_{\text{cool}}/t_{\text{ff}}$ ratio as a function of halo mass at a common radius of $0.1 R_{\text{vir}}$ for our optimal model for the energy loading found in Section 3.3. Generally, if we were to evaluate it at small radii, the ratio would be lower (although this depends on the density and temperature profiles we adopt).

We find that $t_{\text{cool}}/t_{\text{ff}}$ is somewhat larger than the canonical precipitation prediction in low-mass galaxies, approaching values of $\sim 30-40$, but this ratio drops with increasing halo mass, reaching ratios close to $t_{\text{cool}}/t_{\text{ff}} \simeq 10$ for MW-mass halos. The long cooling times in the low-mass halos seen in our model arise because of the high energy loading (and low mass loading) in the galactic winds from SNe. This raises the CGM temperature well above the virial temperature and makes the CGM strongly overpressurized, as well as lowering the CGM density due to high mass and energy outflows out of the halo. The amount of energy and mass lifted out of the CGM is sensitive to what we assume for the specific energy of these outflows, which is not well understood. For simplicity, we assume that the specific energy of these halo outflows is equal

to the average specific energy of the entire CGM, but this need not be the case in real galaxies, where it is possible that the gas lifted out of the halo could have a much higher specific energy. Such outflows would lower the average temperature in the CGM and potentially bring the remaining gas closer to the precipitation picture than what our model predicts for low-mass halos.

Our ratios for $t_{\text{cool}}/t_{\text{ff}}$ can also be compared with certain cooling-flow models of the CGM, where ineffective heating allows cool gas to cascade inward on a cooling timescale (Stern et al. 2019). Such models for a MW-mass halo also find ratios between t_{cool} and t_{ff} that approach $\sim 7\text{--}10$ when gas accretion and the star formation are approximately equal. Such cooling-flow models also predict shorter cooling times in lower-mass halos, which is in contrast to our model, where energy outflows from SNe in these galaxies is very effective at heating the CGM and constraining gas accretion.

4.4. Comparison to Other Regulator Models

Similar analytic regulator models in the past have also considered treatments of preventative and ejective feedback. Although they do not explicitly solve for the CGM reservoir, Davé et al. (2012) included a preventative feedback parameter to quantify the amount of gas that enters the halo but is prevented from reaching the ISM. This preventative feedback includes not only contributions from winds but also photo-ionization, quenching, and virial shocks. Although their inclusion of preventative feedback is largely illustrative, they do converge onto a picture of preventative feedback being a stronger contributor that limits gas accretion in lower-mass galaxies ($\sim 10^9 M_{\odot}$) and declining in importance for more massive halos.

The key differences between our regulator model and past constructions lie in determining how feedback processes set the stellar-to-halo mass relation and its low-mass-end slope. Lilly et al. (2013) find with their gas-regulator model that $\sim 40\%$ of baryons that flow into the halos of galaxies across a stellar mass range from 10^9 to $10^{11} M_{\odot}$ are processed within galaxies. Their fit to Sloan Digital Sky Survey data from Mannucci et al. (2010) yield η_M values of 0.2–0.3 for $M_{\star} = 10^{10} M_{\odot}$ systems, which are comparable to the values assumed in this work for similar systems, but this agreement would not be true for lower-mass systems due to the steep inverse dependence between the mass-loading factor and stellar mass required in their fit to match the data. The equilibrium model used in Mitra et al. (2015), employing a similar preventative feedback scheme to Davé et al. (2012) and fitting η_M to galaxy scaling relations, finds $\eta_M \propto M_{\star}^{-0.5}$, not much larger than our $\beta = 0.5$ scaling, however progressively larger mass outflows are required to match observations at higher redshift. More recent work, from Mitchell & Schaye (2022), built a regulator-like model based on reproducing the flow terms from the EAGLE cosmological simulation, finding ejective feedback out of galaxies and halos to be the primary process shaping the stellar-to-halo mass relation, although with preventative feedback also playing a significant role. High mass loadings, particularly in low-mass galaxies, are a persistent feature of most galactic regulator models, which makes our model, accounting for the energy content of the CGM and self-consistent treatment of preventative feedback, a significant departure from past regulator models.

Other preventative feedback models have placed the location of galaxy regulation in the IGM, where preheating in the IGM prevents a portion of baryons from collapsing into halos due to their enhanced thermal pressure (Lu et al. 2015a). These models rely predominantly on preventative feedback with low-mass loading at late times, and have also found some success in matching certain galaxy scaling relations, such as the size evolution of galactic disks (Lu et al. 2015b) and the mass–metallicity relation of low-mass galaxies (Lu et al. 2017).

This relates to other sources of preventative feedback that could come from the larger ecosystem in which galaxies are themselves embedded. Gas within group and cluster environments that accretes into halos may possess physical properties that prevent its cooling and accretion into galaxies but are not directly connected to the internal feedback of the galaxy itself. The environment may affect the overall gas content of galaxies, as well, where lower-mass satellite galaxies moving through the halos of much larger hosts or galaxy systems can have the gas content of their CGM and ISM diminished through ram-pressure and/or tidal stripping, or even have the accretion of new gas cut off entirely (Brown et al. 2017). The roles each of these preventative mechanisms named above (or others) play in regulating star formation and their interactions with one another remains largely unexplored territory in galactic modeling.

In our model of the energy regulation of the CGM, we left out nonthermal contributions to the energy, but the CGM is also home to a significant kinetic energy reservoir. This kinetic energy may manifest as turbulence or bulk flows, which may provide their own form of pressure support against gravity in the CGM that is not entirely thermal (Fielding et al. 2017; Lochhaas et al. 2023). Incorporating this kinetic energy component is the subject of a companion paper (Pandya et al. 2022). In addition, cosmic rays can potentially operate as a preventative mechanism in the CGM, but we leave this for later work.

5. Summary and Conclusion

Wind outflows driven by SNe are a powerful mechanism for regulating the baryonic contents of galaxies. We adopt a simple gas-regulator model to understand how different mass and energy wind loading factors affect the global properties of galaxies and their scaling relations. We include the CGM as a reservoir, adopting a simple radial density profile, and track the flows of mass, metallicity, and energy, along with the ISM mass and its metallicity and the stellar mass of the central galaxy. We run the regulator model over a halo mass range of $\log M_{\text{halo}}/M_{\odot} = 10\text{--}12$ and compare the galaxy properties at the present day to a set of galaxy scaling relations. The major conclusions of our work are described below:

1. A gas-regulator model tracking the flows of mass, metallicity, and energy in and out of the CGM reservoir is able to qualitatively reproduce the broad features of galaxy scaling relations such as the $M_{\star}/M_{\text{h}}\text{--}M_{\text{h}}$ relation and the $M_{\text{ISM}}/M_{\star}\text{--}M_{\star}$ relation over the range $\log M_{\text{halo}}/M_{\odot} = 10\text{--}12$, where SNe are believed to be the dominant source of baryonic feedback.
2. The estimated stellar mass near the present-day redshift is robust against choices for η_M and η_Z , but is sensitive to the value of η_E , suggesting that preventative feedback from energetic outflows could play a significant role in limiting subsequent gas accretion into the ISM. High-energy-loaded winds heat the CGM and lift heated gas

out of the halo, reducing the density of the CGM and suppressing cosmic infall from the IGM. This limits the cooling efficiency of the CGM and accretion to the ISM. The $M_*/M_h - M_h$ relation favors increasing values of η_E for decreasing M_h , where $\eta_E \sim 1$ for $10^{10} M_\odot$ mass halos and ~ 0.1 for MW-like halos.

3. The CGM plays a significant role in regulating mass outflows from the galaxy when the CGM is overpressurized. Highly mass-loaded outflows from the galaxy increase the mass and density of the CGM and lower the CGM's specific energy, inhibiting its ability to suppress cosmic inflow from the IGM. These processes enhance future accretion from the CGM through shortening the cooling timescale and enables the rapid accretion of gas back into the ISM.
4. Our model of a hot CGM with a radial density profile going as $\propto r^{-1.4}$ produces mass estimates of the CGM that are comparable to the mass in the ISM and stellar component, and broadly consistent with observational constraints on the mass of the MW's CGM. The mass and metallicity of the CGM is strongly linked to the composition of galactic outflows.
5. Larger values of η_M increase the mass left over in the CGM reservoir by the present day, whereas greater η_E and η_Z diminish the CGM mass through lifting heated gas out of the halo and enhancing accretion from radiative cooling, respectively.
6. SNe-driven winds regulate the cooling efficiency of the CGM, and the relation between the cooling time, t_{cool} , and the freefall time, t_{ff} , of circumgalactic gas. When evaluating $t_{\text{cool}}/t_{\text{ff}}$ at a common radius of $0.1 R_{\text{vir}}$, the value of $t_{\text{cool}}/t_{\text{ff}}$ is largest in the CGM of low-mass halos, reaching as high as 30–40 due to very effective heating from SNe, which raises the CGM temperature well above the virial temperature. The ratio $t_{\text{cool}}/t_{\text{ff}}$ decreases with increasing halo mass and approaches the predicted ratio from precipitation and cooling-flow models of ≈ 10 in MW-like halos.
7. Feedback through strong mass ejection from the ISM alone is unable to reproduce the $M_*/M_h - M_h$ relation in the scenario where material ejected from the galaxy is deposited to the CGM, unless the mass loadings in low-mass galaxies are considerably larger than those considered in this work. It is sufficient, however, in the (more extreme) scenario in which the ejected gas is delivered directly to the IGM.

G.L.B. acknowledges support from the NSF (AST-2108470, XSEDE grant No. MCA06N030), NASA TCAN grant No. 80NSSC21K1053, and the Simons Foundation (grant No. 822237). Support for this work was provided by NASA through the NASA Hubble Fellowship grant No. HST-HF2-51489 awarded by the Space Telescope Science Institute, which is operated by the Association of Universities for Research in Astronomy, Inc., for NASA, under contract NAS5-26555. R.S.S. is supported by the Simons Foundation.

Appendix A Interstellar Medium Metallicity Scaling Relations

The regulator model tracks the metallicity evolution of the ISM and CGM, respectively. Although the focus of this work is on the CGM, it can still be insightful to see how the ISM metallicity responds to changes in the composition of outflows, as was done in Section 3.2 for other properties. Figure A1 displays the ISM metallicity as a fraction of the solar metallicity, Z_{ISM}/Z_\odot , as a function of halo mass for different choices of outflow parameters, starting from the same initial set chosen in Section 3.2, where $\eta_M = 1$, $\eta_E = 0.3$, and $\eta_Z = 0.5$, respectively.

In the leftmost plot, where we vary the mass loading, we find that the ISM metallicity decreases with larger values of η_M but that this difference is more pronounced in larger halos. Increasing η_M ejects more metals out of the galaxy, while at the same time reducing the overall star formation (although not by much when the CGM is overpressurized, as discussed in Section 3.2.1). The trend begins to flatten at different halo masses depending on the choice of η_M , mirroring the behavior seen in the CGM metallicity and stellar mass when the CGM is no longer overpressurized.

Energy loading can also change the ISM metallicity, as shown in the middle panel. Larger η_E reduces the overall star formation in the galaxy by limiting accretion of gas from the CGM, a source term for metals in the ISM. High energy loading reduces the ISM metallicity across almost all halo masses, except in the lowest-mass galaxies.

Lastly, in the rightmost plot, the metal-loading factor adjusts the fraction of metals which leave the ISM in the wind, and has the most direct effect on the ISM metallicity. Increasing η_Z has the expected result of directly reducing the metallicity of the gas left in the galaxy, changing Z_{ISM} from being roughly equal to the solar metallicity in the MW-like systems when $\eta_Z = 0.1$ to $Z_{\text{ISM}} \sim 0.25 Z_\odot$ when $\eta_Z = 1$.

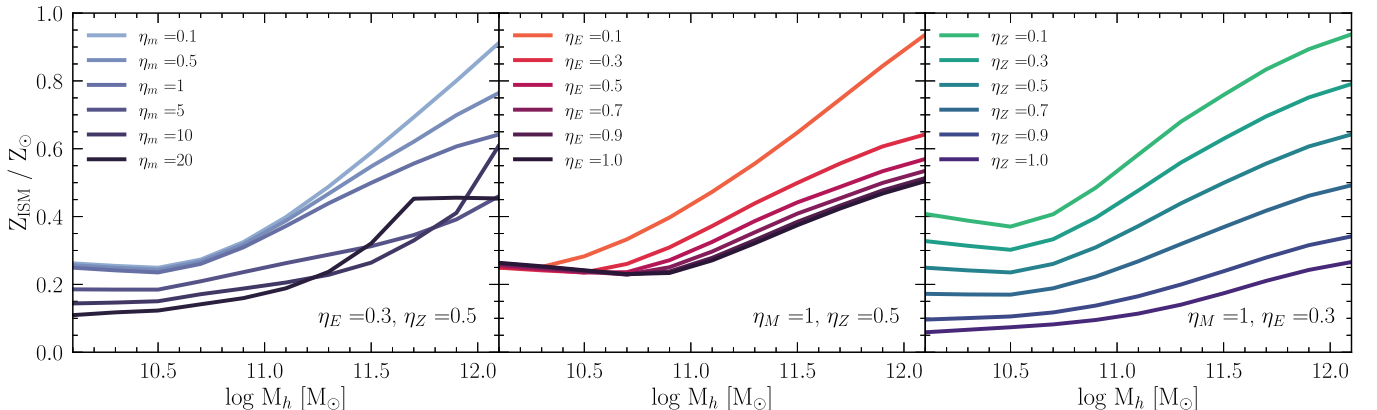


Figure A1. ISM metallicity as a fraction of solar metallicity as a function of halo mass. Estimates of Z_{ISM}/Z_\odot are presented as a function of wind mass loading η_M (left), energy loading η_E (middle), and metal loading η_Z (right). The annotations of each plot display which parameters were kept constant in the iterations of the model on display.

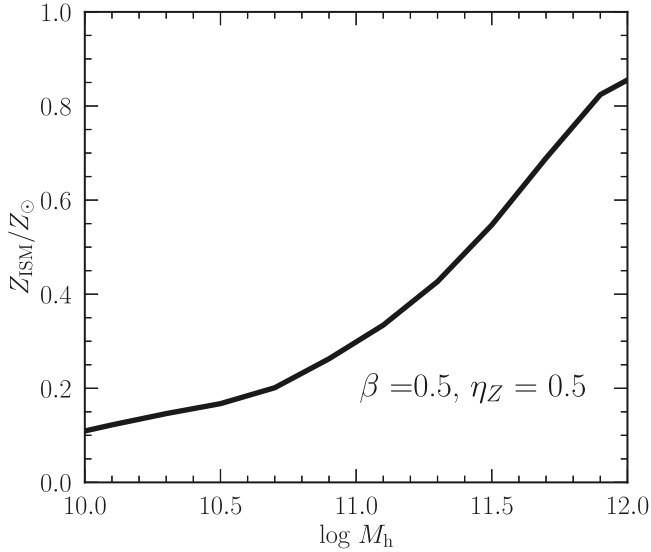


Figure A2. ISM metallicity as a fraction of solar metallicity as a function of halo mass. We use the optimal values from η_E taken from the recursive bisection fit to the Behroozi et al. (2019) M_*/M_h - M_h relation in Section 3.3.

After showing how Z_{ISM}/Z_{\odot} varies as we change outflow parameters, we display in Figure A2 how the ISM metallicity evolves as a function of halo mass for our best-fit η_E values from the recursive bisection fit to the Behroozi et al. (2019) M_*/M_h - M_h relation in Section 3.3, assuming the same power-law relation of η_M with halo mass in Equation (22), with $\beta=0.5$ and $\eta_Z=0.5$. Unsurprisingly, we find that ISM metallicity increases for larger halo masses, with $Z_{\text{ISM}}/Z_{\odot} \sim 0.1$ for the lowest-mass dwarfs and ~ 0.85 for MW-like halos. Although this is far from a complete model of the metal content of galaxies, the ISM metallicity responds as expected to changes in the composition of outflows within the context of the model and reproduces basic trends in enrichment as a function of halo mass expected in real galaxies (Andrews & Martini 2013).

Appendix B Depletion Time Sensitivity

Here we test the sensitivity of our regulator model to assumed parameters outside our characterization of wind outflows. First, the depletion time sets the timescale for the conversion of gas into stars. This conversion is observed to be more efficient in MW-

mass galaxies (i.e., higher stellar masses). This is expressed in Equation (13) as used for t_{dep} and referenced in Section 2.2.4. We can modulate the normalization of t_{dep} and its power-law dependence. In prior sections, we used the depletion time estimate derived from McGaugh et al. (2017), where the logarithmic depletion time is normalized by a prefactor equal to 4.92 and a dependence on stellar mass with a power-law index of 0.37. We define the normalization of depletion time as a parameter called C and its power-law index as γ . For this section, we keep one parameter set to its fiducial value while varying the other. Since the influence of t_{dep} should primarily cover the conversion of gas into stars in the galaxy, we place a special emphasis on the M_*/M_h - M_h relation and the M_{ISM}/M_* - M_* relation. For these tests, as well as those in Appendix C, for the fiducial model we use the power-law formula dependent on halo mass introduced in Equation (22) with a power-law index of $\beta=0.5$, the power-law fit of η_E from Equation (23) and its best-fit values, and set $\eta_Z=0.5$.

We show in the left-hand plot of Figure B1 that modulating the normalization of t_{dep} over an order of magnitude from $C=4.25$ - 5.5 does have a noticeable effect on the M_*/M_h - M_h relation, such that larger (smaller) values result in reduced (greater) stellar masses, especially in more massive halos. This is partly to be expected, considering that a larger normalization would lead to larger depletion timescales and a reduced star formation rate. The less efficient conversion of gas into stars leads a greater proportion of gas to stars in all galaxies as a function of halo mass, manifesting as a vertical shift in the M_{ISM}/M_* - M_* relation of the model (left-hand plot of Figure B2).

The right-hand plot of Figure B1 shows how modifying the power-law index of t_{dep} has very little effect on the M_*/M_h - M_h relation. The most apparent consequence of modifying γ is seen in Figure B2, where it is shown that the power-law index of the depletion time alters the slope of the M_{ISM}/M_* - M_* relation produced by the model. Increasing the index reduces the star formation efficiency in low-mass halos and increases its efficiency in more massive halos and vice versa for its reduction. Larger values of γ are in better agreement with the slope of the power-law fit from Calet et al. (2018), with $\gamma \geq 0.5$ producing the closest match with their observational constraints.

The robustness of the stellar mass to the power-law dependence of the depletion time and even its normalization at the lower-mass end in Figure B1 may point to the important role that t_{dep} plays in setting the timescale for self-regulation to arise at high redshift. Longer depletion times, especially in low-mass halos, delay the

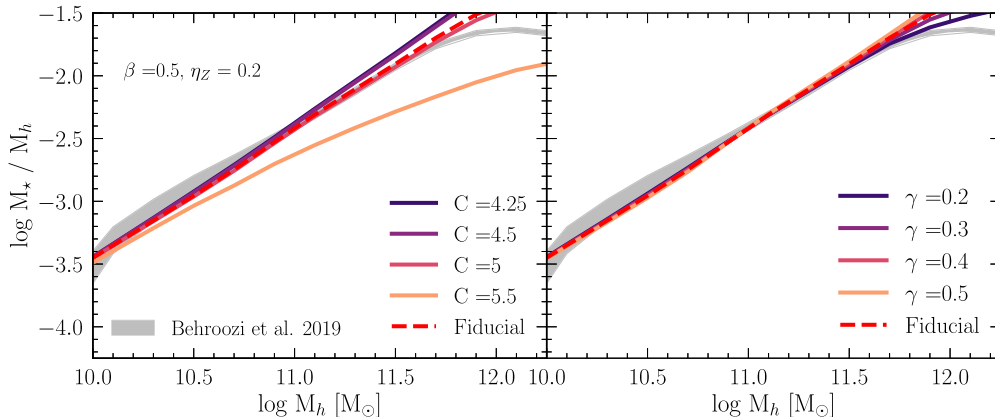


Figure B1. Log of M_*/M_h from the regulator model as a function of halo mass, compared to the median observed stellar mass with uncertainties in gray and their derived halo mass from abundance matching from Behroozi et al. (2019). Estimates of M_*/M_h are presented as a function of the normalization of the depletion time C (left), and its power-law dependence γ (right).

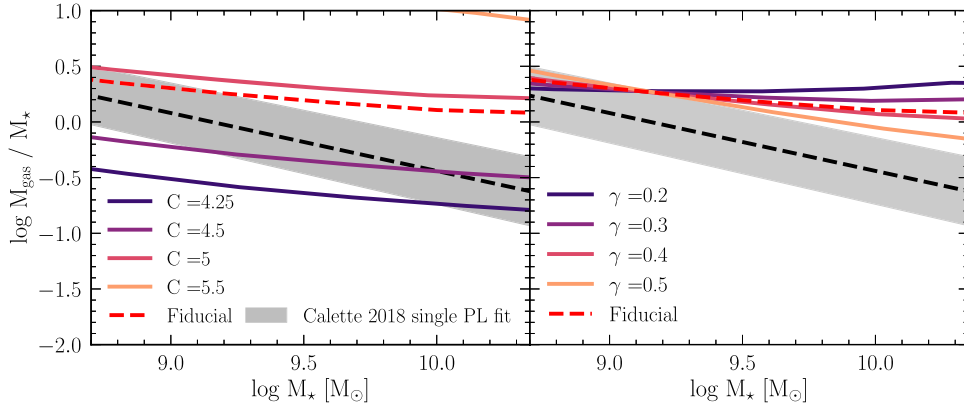


Figure B2. Log of M_{ISM}/M_* from the regulator model as a function of stellar mass, compared to the best-fit single power-law fit for the total cold gas mass as a function of M_* over the range $7.3 \lesssim \log(M_*/M_h) \lesssim 11.2$ for late-type galaxies from Calette et al. (2018). Shaded lines correspond to alterations in the normalization of the depletion time C (left) and its power-law dependence with stellar mass γ (right) and their respective influence on the $M_{\text{ISM}}-M_*$ relation.

ignition of star formation and the high-specific-energy outflows that prevent accretion into the CGM and the ISM. This means that, although star formation in the disk becomes less efficient, the increased baryon fraction in the halo leaves the resulting stellar mass largely unchanged. Shorter depletion times in low-mass halos (i.e., lower power-law index) means that they are more efficient in their star production, but suppress cosmic inflow through self-regulation much earlier, leaving less gas in the galaxy to be processed into stars.

Appendix C Density Profile Sensitivity

Another important quantity in our model is our assumed density profile of the CGM. In Equation (1), we assume a power-law dependence with distance from the center with an index of $\alpha = 1.4$. Since the density profile of the CGM is not well constrained, it is important to observe how our models respond to different assumptions of the gas density profile. Varying α in our parameterization of the density profile changes how $\rho(r)$ depends

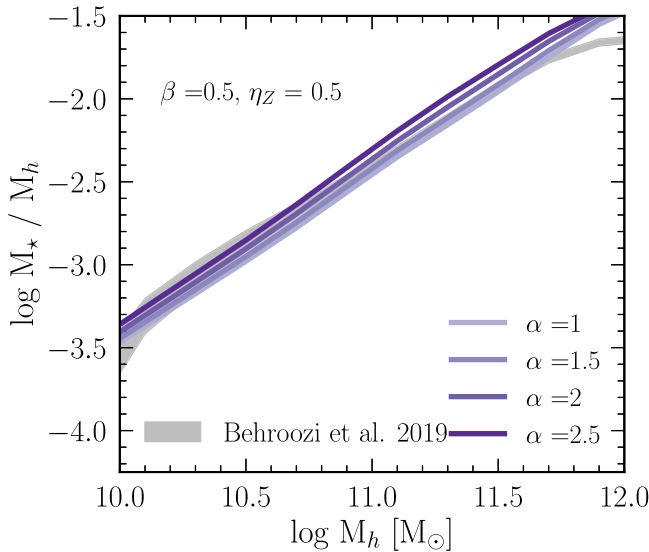


Figure C1. Log of M_*/M_h from the regulator model as a function of halo mass compared to the median observed stellar mass, with uncertainties in gray and their derived halo mass from abundance matching from Behroozi et al. (2019). Shaded lines represent different variations of the power-law index for the CGM radial density profile α and its effect on the M_*/M_h-M_h relation.

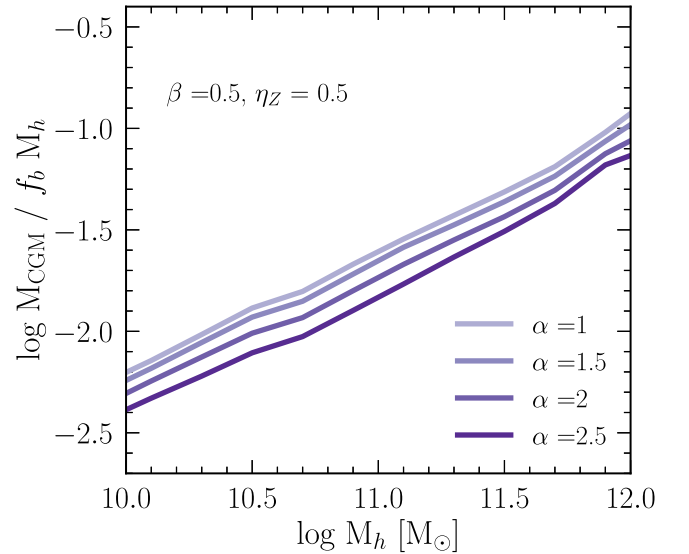


Figure C2. Estimates of $\log(M_{\text{CGM}}/M_h)$ as a function of halo mass. Estimates of M_{CGM}/M_h are presented as a function of the power-law index for the CGM radial density profile α .

on radius, where larger values of α produce a steeper density profile and where a greater concentration of gas is placed in the inner CGM relative to its outskirts.

After plotting the M_*/M_h-M_h relation for varying forms of the CGM density profile in Figure C1, we find that larger values of α increase the stellar mass at $z = 0$ for all halos. With a greater concentration of mass in the inner CGM, steeper density profiles elevate the overall cooling efficiency of gas near the galaxy and result in greater accretion and more fuel for star formation. This rise in star formation should also work to increase the total outflow of energy into the CGM, but this countering response to enhanced accretion is not enough to fully oppose the significant radiative losses in the inner gas halo. Steeper density profiles have a predictable effect on the CGM. In Figure C2, larger values of α result in less mass in the CGM at late times due to the greater accretion from the CGM to the ISM.

ORCID iDs

Christopher Carr <https://orcid.org/0000-0002-5840-0424>
Greg L. Bryan <https://orcid.org/0000-0003-2630-9228>

Drummond B. Fielding  <https://orcid.org/0000-0003-3806-8548>

Viraj Pandya  <https://orcid.org/0000-0002-2499-9205>

Rachel S. Somerville  <https://orcid.org/0000-0002-6748-6821>

References

- Andrews, B. H., & Martini, P. 2013, *ApJ*, **765**, 140
- Anglés-Alcázar, D., Faucher-Giguère, C.-A., Kereš, D., et al. 2017, *MNRAS*, **470**, 4698
- Asplund, M., Grevesse, N., Sauval, A. J., & Scott, P. 2009, *ARA&A*, **47**, 481
- Baugh, C. M. 2006, *RPPh*, **69**, 3101
- Behroozi, P., Wechsler, R. H., Hearin, A. P., & Conroy, C. 2019, *MNRAS*, **488**, 3143
- Benson, A. J. 2010, *PhR*, **495**, 33
- Benson, A. J., & Bower, R. 2011, *MNRAS*, **410**, 2653
- Benson, A. J., Bower, R. G., Frenk, C. S., et al. 2003, *ApJ*, **599**, 38
- Birrer, S., Lilly, S., Amara, A., Paranjape, A., & Refregier, A. 2014, *ApJ*, **793**, 12
- Bland-Hawthorn, J., & Gerhard, O. 2016, *ARA&A*, **54**, 529
- Bouche, N., Dekel, A., Genzel, R., et al. 2010, *ApJ*, **718**, 1001
- Bregman, J. N. 1980, *ApJ*, **236**, 577
- Brown, T., Catinella, B., Cortese, L., et al. 2017, *MNRAS*, **466**, 1275
- Calette, A. R., Avila-Reese, V., Rodríguez-Puebla, A., Hernández-Toledo, H., & Papastergis, E. 2018, *RMxAA*, **54**, 443
- Chisholm, J., Tremonti, C. A., Leitherer, C., & Chen, Y. 2017, *MNRAS*, **469**, 4831
- Cole, S., Lacey, C. G., Baugh, C. M., & Frenk, C. S. 2000, *MNRAS*, **319**, 168
- Collins, M. L. M., & Read, J. I. 2022, *NatAs*, **6**, 647
- Concas, A., Maiolino, R., Curti, M., et al. 2022, *MNRAS*, **513**, 2535
- Cousin, M., Lagache, G., Bethermin, M., & Guiderdoni, B. 2015, *A&A*, **575**, A33
- Crain, R. A., Schaye, J., Bower, R. G., et al. 2015, *MNRAS*, **450**, 1937
- Croton, D. J., Springel, V., White, S. D. M., et al. 2006, *MNRAS*, **365**, 11
- Das, S., Mathur, S., Gupta, A., & Krongold, Y. 2021, *ApJ*, **918**, 83
- Davé, R., Anglés-Alcázar, D., Narayanan, D., et al. 2019, *MNRAS*, **486**, 2827
- Davé, R., Finlator, K., & Oppenheimer, B. D. 2012, *MNRAS*, **421**, 98
- Dekel, A., Birnboim, Y., Engel, G., et al. 2009, *Natur*, **457**, 451
- Dekel, A., & Mandelker, N. 2014, *MNRAS*, **444**, 2071
- Dekel, A., & Silk, J. 1986, *ApJ*, **303**, 39
- Dekel, A., Zolotov, A., Tweed, D., et al. 2013, *MNRAS*, **435**, 999
- Donahue, M., & Voit, G. M. 2022, *PhR*, **973**, 1
- Esmerian, C. J., Kravtsov, A. V., Hafen, Z., et al. 2021, *MNRAS*, **505**, 1841
- Faerman, Y., Pandya, V., Somerville, R. S., & Sternberg, A. 2022, *ApJ*, **928**, 37
- Faerman, Y., Sternberg, A., & McKee, C. F. 2020, *ApJ*, **893**, 82
- Fielding, D., Quataert, E., & Martizzi, D. 2018, *MNRAS*, **481**, 3325
- Fielding, D., Quataert, E., McCourt, M., & Thompson, T. A. 2017, *MNRAS*, **466**, 3810
- Fielding, D. B., Tonnesen, S., DeFelippis, D., et al. 2020, *ApJ*, **903**, 32
- Finlator, K., & Davé, R. 2008, *MNRAS*, **385**, 2181
- Ford, A. B., Davé, R., Oppenheimer, B. D., et al. 2014, *MNRAS*, **444**, 1260
- Fraternali, F., Marasco, A., Armillotta, L., & Marinacci, F. 2015, *MNRAS*, **447**, L70
- Furlanetto, S. R. 2021, *MNRAS*, **500**, 3394
- Furlanetto, S. R., & Mirocha, J. 2022, *MNRAS*, **511**, 3895
- Girichidis, P., Walch, S., Naab, T., et al. 2016, *MNRAS*, **456**, 3432
- Heckman, T. M., Armus, L., & Miley, G. K. 1990, *ApJS*, **74**, 833
- Heitsch, F., & Putman, M. E. 2009, *ApJ*, **698**, 1485
- Hou, J., Lacey, C. G., & Frenk, C. S. 2018, *MNRAS*, **475**, 543
- Hu, C.-Y. 2019, *MNRAS*, **483**, 3363
- Kauffmann, G., White, S. D. M., & Guiderdoni, B. 1993, *MNRAS*, **264**, 201
- Kereš, D., Katz, N., Davé, R., Fardal, M., & Weinberg, D. H. 2009, *MNRAS*, **396**, 2332
- Kim, C.-G., Ostriker, E. C., & Raileanu, R. 2017, *ApJ*, **834**, 25
- Kim, C.-G., Ostriker, E. C., Somerville, R. S., et al. 2020, *ApJ*, **900**, 61
- Kroupa, P. 2001, *MNRAS*, **322**, 231
- Krumholz, M. R., McKee, C. F., & Tumlinson, J. 2009, *ApJ*, **699**, 850
- Li, M., & Bryan, G. L. 2020, *ApJL*, **890**, L30
- Li, M., Bryan, G. L., & Ostriker, J. P. 2017, *ApJ*, **841**, 101
- Li, M., & Tonnesen, S. 2020, *ApJ*, **898**, 148
- Lilly, S. J., Carollo, C. M., Pipino, A., Renzini, A., & Peng, Y. 2013, *ApJ*, **772**, 119
- Lochhaas, C., Tumlinson, J., Peeples, M. S., et al. 2023, *ApJ*, **948**, 43
- Lu, Y., Benson, A., Wetzel, A., et al. 2017, *ApJ*, **846**, 66
- Lu, Y., Kereš, D., Katz, N., et al. 2011, *MNRAS*, **416**, 660
- Lu, Y., Mo, H. J., & Lu, Z. 2015a, arXiv:1504.02109
- Lu, Y., Mo, H. J., & Wechsler, R. H. 2015b, *MNRAS*, **446**, 1907
- Maller, A. H., & Bullock, J. S. 2004, *MNRAS*, **355**, 694
- Mannucci, F., Cresci, G., Maiolino, R., Marconi, A., & Gnerucci, A. 2010, *MNRAS*, **408**, 2115
- Marasco, A., Belfiore, F., Cresci, G., et al. 2023, *A&A*, **670**, A92
- Marasco, A., Fraternali, F., Lehner, N., & Howk, J. C. 2022, *MNRAS*, **515**, 4176
- Martin, C. L. 1999, *ApJ*, **513**, 156
- McCourt, M., Sharma, P., Quataert, E., & Parrish, I. J. 2012, *MNRAS*, **419**, 3319
- McGaugh, S. S., Schombert, J. M., & Lelli, F. 2017, *ApJ*, **851**, 22
- McQuinn, K. B. W., van Zee, L., & Skillman, E. D. 2019, *ApJ*, **886**, 74
- Mitchell, P. D., & Schaye, J. 2022, *MNRAS*, **511**, 2948
- Mitra, S., Davé, R., & Finlator, K. 2015, *MNRAS*, **452**, 1184
- Moster, B. P., Somerville, R. S., Maulbetsch, C., et al. 2010, *ApJ*, **710**, 903
- Muratov, A. L., Kereš, D., Faucher-Giguère, C.-A., et al. 2015, *MNRAS*, **454**, 2691
- Muratov, A. L., Kereš, D., Faucher-Giguère, C.-A., et al. 2017, *MNRAS*, **468**, 4170
- Naab, T., & Ostriker, J. P. 2017, *ARA&A*, **55**, 59
- Nelson, D., Genel, S., Pillepich, A., et al. 2016, *MNRAS*, **460**, 2881
- Nelson, D., Pillepich, A., Springel, V., et al. 2019, *MNRAS*, **490**, 3234
- Oppenheimer, B. D., & Davé, R. 2006, *MNRAS*, **373**, 1265
- Oppenheimer, B. D., & Davé, R. 2008, *MNRAS*, **387**, 577
- Oppenheimer, B. D., Davé, R., Kereš, D., et al. 2010, *MNRAS*, **406**, 2325
- Ostriker, E. C., & Kim, C.-G. 2022, *ApJ*, **936**, 137
- Pandya, V., Fielding, D. B., Anglés-Alcázar, D., et al. 2021, *MNRAS*, **508**, 2979
- Pandya, V., Fielding, D. B., Bryan, G. L., et al. 2022, arXiv:2211.09755
- Pandya, V., Somerville, R. S., Anglés-Alcázar, D., et al. 2020, *ApJ*, **905**, 4
- Peng, Y.-j., & Maiolino, R. 2014, *MNRAS*, **443**, 3643
- Pillepich, A., Springel, V., Nelson, D., et al. 2018, *MNRAS*, **473**, 4077
- Prochaska, J. X., Werk, J. K., Worseck, G., et al. 2017, *ApJ*, **837**, 169
- Putman, M., Peek, J., & Jounge, M. 2012, *ARA&A*, **50**, 491
- Rupke, D. S. N. 2018, *Galax*, **6**, 138
- Salem, M., Besla, G., Bryan, G., et al. 2015, *ApJ*, **815**, 77
- Schaye, J., Crain, R. A., Bower, R. G., et al. 2014, *MNRAS*, **446**, 521
- Shapiro, P. R., & Field, G. B. 1976, *ApJ*, **205**, 762
- Sharma, P., McCourt, M., Parrish, I. J., & Quataert, E. 2012a, *MNRAS*, **427**, 1219
- Sharma, P., McCourt, M., Quataert, E., & Parrish, I. J. 2012b, *MNRAS*, **420**, 3174
- Somerville, R. S., & Davé, R. 2015, *ARA&A*, **53**, 51
- Somerville, R. S., Hopkins, P. F., Cox, T. J., Robertson, B. E., & Hernquist, L. 2008, *MNRAS*, **391**, 481
- Somerville, R. S., & Primack, J. R. 1999, *MNRAS*, **310**, 1087
- Stern, J., Fielding, D., Faucher-Giguère, C.-A., & Quataert, E. 2019, *MNRAS*, **488**, 2549
- Stern, J., Fielding, D., Faucher-Giguère, C.-A., & Quataert, E. 2020, *MNRAS*, **492**, 6042
- Strickland, D. K., & Heckman, T. M. 2009, *ApJ*, **697**, 2030
- Strickland, D. K., & Stevens, I. R. 2000, *MNRAS*, **314**, 511
- Thompson, T. A., Quataert, E., & Murray, N. 2005, *ApJ*, **630**, 167
- Tripp, T. M., Meiring, J. D., Prochaska, J. X., et al. 2011, *Sci*, **334**, 952
- Tumlinson, J., Peeples, M. S., & Werk, J. K. 2017, *ARA&A*, **55**, 389
- Veilleux, S., Cecil, G., & Bland-Hawthorn, J. 2005, *ARA&A*, **43**, 769
- Vogelsberger, M., Genel, S., Springel, V., et al. 2014, *Natur*, **509**, 177
- Vogelsberger, M., Marinacci, F., Torrey, P., & Puchwein, E. 2020, *NatRP*, **2**, 42
- Voit, G. M., Bryan, G. L., O'Shea, B. W., & Donahue, M. 2015a, *ApJL*, **808**, L30
- Voit, G. M., Donahue, M., Bryan, G. L., & McDonald, M. 2015b, *Natur*, **519**, 203
- Voit, G. M., Meece, G., Li, Y., et al. 2017, *ApJ*, **845**, 80
- White, S. D. M., & Frenk, C. S. 1991, *ApJ*, **379**, 52
- White, S. D. M., & Rees, M. J. 1978, *MNRAS*, **183**, 341
- Wiersma, R. P. C., Schaye, J., & Smith, B. D. 2009, *MNRAS*, **393**, 99